nature energy

Article

https://doi.org/10.1038/s41560-022-01189-1

Metal oxide barrier layers for terrestrial and space perovskite photovoltaics

Received: 13 May 2022

Accepted: 12 December 2022

Published online: 26 January 2023

Check for updates

Ahmad R. Kirmani[1] ✉, David P. Ostrowski[1], Kaitlyn T. VanSant[1,2], Todd A. Byers[3], Rosemary C. Bramante[1], Karen N. Heinselman[1], Jinhui Tong[1], Bart Stevens[1], William Nemeth[1], Kai Zhu[1], Ian R. Sellers[4], Bibhudutta Rout[3] & Joseph M. Luther[1] ✉

Perovskite photovoltaics are attractive for both terrestrial and space applications. Although terrestrial conditions require durability against stressors such as moisture and partial shading, space poses different challenges: radiation, atomic oxygen, vacuum and high-temperature operation. Here we demonstrate a silicon oxide layer that hardens perovskite photovoltaics to critical space stressors. A 1-µm-thick silicon oxide layer evaporated atop the device contacts blocks 0.05 MeV protons at fluences of 10^{15} cm^{-2} without a loss in power conversion efficiency, which results in a device lifetime increase in low Earth orbit by ×20 and in highly elliptical orbit by ×30. Silicon-oxide-protected $Cs_{0.05}(MA_{0.17}FA_{0.83})_{0.95}Pb(I_{0.83}Br_{0.17})_3$ (MA, methylammonium; FA, formamidinium cation) and $CsPbI_2Br$ cells survive submergence in water and *N*,*N*-dimethylformamide. Furthermore, moisture tolerance of Sn-Pb and $CsPbI_2Br$ devices is boosted. Devices are also found to retain power conversion efficiencies on exposure to alpha irradiation and atomic oxygen. This barrier technology is a step towards lightweight packaging designs for both space and terrestrial applications.

Installed solar power in the near-Earth space is expected to grow exponentially over the next decade and approach 1 GW from the current value of a few MWs[1]. As the internet-of-space becomes a reality[2], projects such as SpaceX Starlink, Amazon's Project Kuiper and OneWeb of the UK government aim to launch a total of ~100,000 satellites into low Earth orbit (LEO)[1]. Interest is also rising in harnessing solar energy from space and beaming it down to Earth to power the electric grid by installing space-based solar cells in highly elliptical orbits[3,4]. This rapid penetration of space necessitates a low-cost lightweight solar power technology that is resilient to challenges faced by electronics in space, which include radiation, thermal cycling, atomic oxygen and high vacuum.

Metal halide perovskites are a potential next-generation space photovoltaic (PV) technology with a high tolerance to radiation compared with that of existing technology. Presently, a comprehensive assessment of the hardness across all space stressors is still needed for the many perovskite solar cell structures and various implementations[1,5–9]. The space environment poses a very different set of challenges compared to those for terrestrial deployment[10]. Although exposure to weather, notably moisture, is not a major concern, radiation, ultraviolet photons and atomic oxygen form major stressors in space and cause atomic defects and performance degradation in semiconductors[11,12]. Nevertheless, space solar panels must tolerate moisture and oxygen during the storage and launch phases. Traditionally, bulky packaging and cover glass are used as radiation shields on space solar panels, but this increases the overall weight and launch costs[8,13]. Space-qualified silicone elastomer encapsulants pose a risk of chemical interaction with the perovskite layers, which results in device degradation (Supplementary Fig. 1). Reports on using oxide and polymer barriers are limited to

[1]National Renewable Energy Laboratory (NREL), Golden, CO, USA. [2]Photovoltaic and Electrochemical Systems Branch, NASA Glenn Research Center, Cleveland, OH, USA. [3]Department of Physics, University of North Texas, Denton, TX, USA. [4]Homer L. Dodge Department of Physics and Astronomy, University of Oklahoma, Norman, OK, USA. ✉e-mail: ahmad.kirmani@rit.edu; joey.luther@nrel.gov

moisture protection and use either costly and time-consuming deposition techniques or costly materials[14–18]. Although cover glasses are traditionally used as a robust barrier technology in space solar cells, they compromise the specific power advantage that the next-generation ultrathin film PV technologies, which include perovskites, offer. Additionally, polymer barriers are likely to degrade under space irradiation given the intolerance of organic species and chemical bonds to these harsh conditions[19]. A lightweight barrier layer technology that can be deposited in a low-cost fashion without chemical interaction with the device stack remains to be demonstrated for perovskite PVs.

In this article, we present an industrially viable metal oxide barrier layer technology for perovskite solar cells. We chose silicon oxide (SiO_x) to demonstrate this concept given its low cost and ease of deposition via thermal evaporation. Theoretical simulations of proton–perovskite interactions pointed towards an optimum thickness of 1 µm to fully block the most damaging low-energy protons in the energy range of ~0.05 MeV. Protons in this low-energy range are abundant in space and can interact throughout the micrometre-thick perovskite device stack. These protons also have a high scattering probability with perovskites causing maximum atomic displacements and vacancies and thus are recommended for validating the radiation hardness of perovskite solar cells[20]. Here, SiO_x was found to improve radiation tolerance such that solar cells exposed to a 10^{15} cm^{-2} fluence of 0.05 MeV protons remained unharmed. Some LEO and highly elliptical orbit missions are expected to experience annual fluences of 10^{13}–10^{14} cm^{-2} of these low-energy protons (Supplementary Fig. 2) (https://www.spenvis.oma.be/). SiO_x was also found to protect the solar cells from higher-energy protons (1 MeV) and alpha particles (α-particles) (2 MeV) that penetrate the barrier layer, probably by suppressing the effusion of volatile chemical species upon irradiation. Exposure of SiO_x-capped cells to atomic oxygen during ultraviolet–ozone (UVO) treatment resulted in no change in the initial power conversion efficiencies (PCEs). Interestingly, we found that the SiO_x barrier also improves the resilience of solar cells to terrestrial stressors—moisture and polar solvents—presenting a wider use than originally envisioned. We specifically tested the resilience of two crucial perovskite absorber chemistries—low bandgap Sn–Pb and wider bandgap $CsPbI_2Br$—which are highly sensitive to moisture but important to tandem PV designs[21–25]. Surprisingly, after a 1 µm layer of SiO_x was added atop these cells, we were able to carry out current density–voltage (*J*–*V*) measurements of Sn–Pb solar cells in the ambient, and $CsPbI_2Br$ solar cells showed no noticeable loss in PCE even after 100 days of storage in the ambient. In fact, the cells survived aggressive submersion in deionized water and N,N-dimethylformamide (DMF), a solvent that readily dissolves the perovskites and is used for deposition. Compared with the conventional cover glass encapsulants, the oxide barrier technology provides a >99% solar array weight reduction, boosts the solar cell specific power from 134 to 277 W kg^{-1}, cuts the encapsulant cost by 99.97% (Supplementary Figs. 3–5) and stands to benefit both the space and terrestrial deployment of perovskite PVs.

Improved radiation tolerance

Protons trapped in the Earth's magnetic field present the greatest hazard to space electronics and solar panels[26]. Protons that possess low energies, such as 0.05 MeV (50 keV), come to rest inside a micrometre-thick device stack, which leads to nuclear displacements[11]. Higher-energy protons are present in fluences several orders of magnitude lower, and have less interaction with the device stack. These protons were recently also shown to result in localized healing of defects in perovskites due to lattice heating via electronic ionization[6]. As such, low-energy protons are a good choice for testing radiation hardness of perovskites. Space solar cells are not tested using these low-energy protons as a standard because it is acknowledged that at least some radiation protection in the form of cover glass is necessary, which blocks these protons. However, for the emerging technologies, which include perovskites, CdTe, and ultrathin III–V semiconductors, the necessity for a cover glass is being questioned given the resilience of the underlying device to fully penetrating protons. By minimizing encapsulation, these next-generation technologies can lead to superior specific powers beyond the reach of conventional space solar cells. It therefore becomes necessary to consider the effect of low-energy protons and develop a solution to blocking them.

We started by simulating the interaction of 0.05 MeV protons with perovskite solar cells using the software SRIM/TRIM (stopping and range of ions in matter/transport of ions in matter), a Monte Carlo simulation that models the passage of ions through matter, considering energy losses via non-ionizing nuclear displacements and electronic ionization[27]. We considered both n-i-p and p-i-n device architectures comprising the standard charge transport layers and perovskite active layer based on $Cs_{0.05}(MA_{0.17}FA_{0.83})_{0.95}Pb(I_{0.83}Br_{0.17})_3$ composition (triple cation), where MA and FA represent methylammonium and the formamidinium cations[28]. Incidence and subsequent traversal of 100,000 protons through the n-i-p architecture (proton straggling) is shown in Fig. 1a,b with and without a 1 µm SiO_x top layer. The total number of vacancies that resulted from the proton interaction are also plotted as a function of depth in the device stack. These lower-energy protons penetrate the device stack and largely create a uniform damage profile through the perovskite absorber layer that resembles the omnidirectional incidence of polyenergetic protons in the space environment. This is different from the case of III–V solar cells in which only high energy protons in the range of MeVs can create a uniform damage profile due to the thickness of these solar cells, which is 3–4 times larger than that of perovskite devices[20,29,30]. Although such a thickness is not a fundamental requirement for the III–V solar cells, it is used for an optimal absorption of the solar spectrum and maximum output power. As such, the damage profile largely depends on the absorber thickness, but tolerance to those vacancies should still be considered. Although protons pass through and create vacancies within the perovskite absorber for the bare solar cell, the SiO_x layer fully blocks them in the SiO_x-capped device without damage to the device stack. We note that the SiO_x layer does not have optical transparency requirements as it is not on the sun-facing side of the device. Proton straggling for the p-i-n triple-cation solar cells is shown in Supplementary Fig. 6.

Encouraged by these theoretical insights, we deposited 1 µm SiO_x on n-i-p and p-i-n solar cells via thermal evaporation and irradiated them with 0.05 MeV protons (Fig. 1c,d). SiO_x deposition did not result in any damage to the devices as evidenced from unchanged PCEs of ~18.5% (Supplementary Fig. 7). Photographs and schematics of the SiO_x encapsulation scheme are shown in Supplementary Fig. 8 and compared with the conventional approach that uses a space-qualified silicon encapsulation. Devices were also exposed to an uncontrolled moisture and temperature environment for several days to mimic the space launch environment and payload integration steps. Devices protected with a 1 µm SiO_x retained their initial 19.0% PCEs whereas

Fig. 1 | SiO*x* as a radiation barrier. a,**b**, Proton straggling in an n-i-p device without (**a**) and with (**b**) a 1-µm-thick SiO_x proton barrier. The total vacancies formed in the device stacks as a function of depth due to proton interaction are shown with red lines. Device schematics are shown for each case, and details on the device architecture are provided in Methods. **c**,**d**, Cross-sectional SEM (X-SEM) images of a representative n-i-p device without (**c**) and with (**d**) an SiO_x layer. **e**,**g**, Average PCEs for n-i-p (**e**) and p-i-n (**g**) devices before and after irradiation with 0.05 MeV protons at fluences of 10^{13} and 10^{15} cm^{-2} without (bare) and with (protected) SiO_x proton barrier. For **e**, averages were performed over four and six devices for the without and with SiO_x cases, respectively. For **g**, averages were performed over six and five devices for the without and with SiO_x cases, respectively. Individual data points are depicted by red circles overlayed on the bars. Error bars represent the s.d. **f**,**h**, Corresponding *J*–*V* curves for the 10^{15} cm^{-2} fluence scenario. Reverse (**f**) and forward (**h**) scans are shown.

https://doi.org/10.1038/s41560-022-01189-1

bare cells degraded from 19.4 to 10.8% due to environmental stressors such as moisture and temperature (Supplementary Fig. 7d,e). We chose proton fluences of 10^{13} and 10^{15} cm^{-2}, which mimic harsh space conditions[20]. We note that the radiation resilience of high-efficiency perovskite solar cells has rarely been tested for such high fluences of low-energy protons[5].

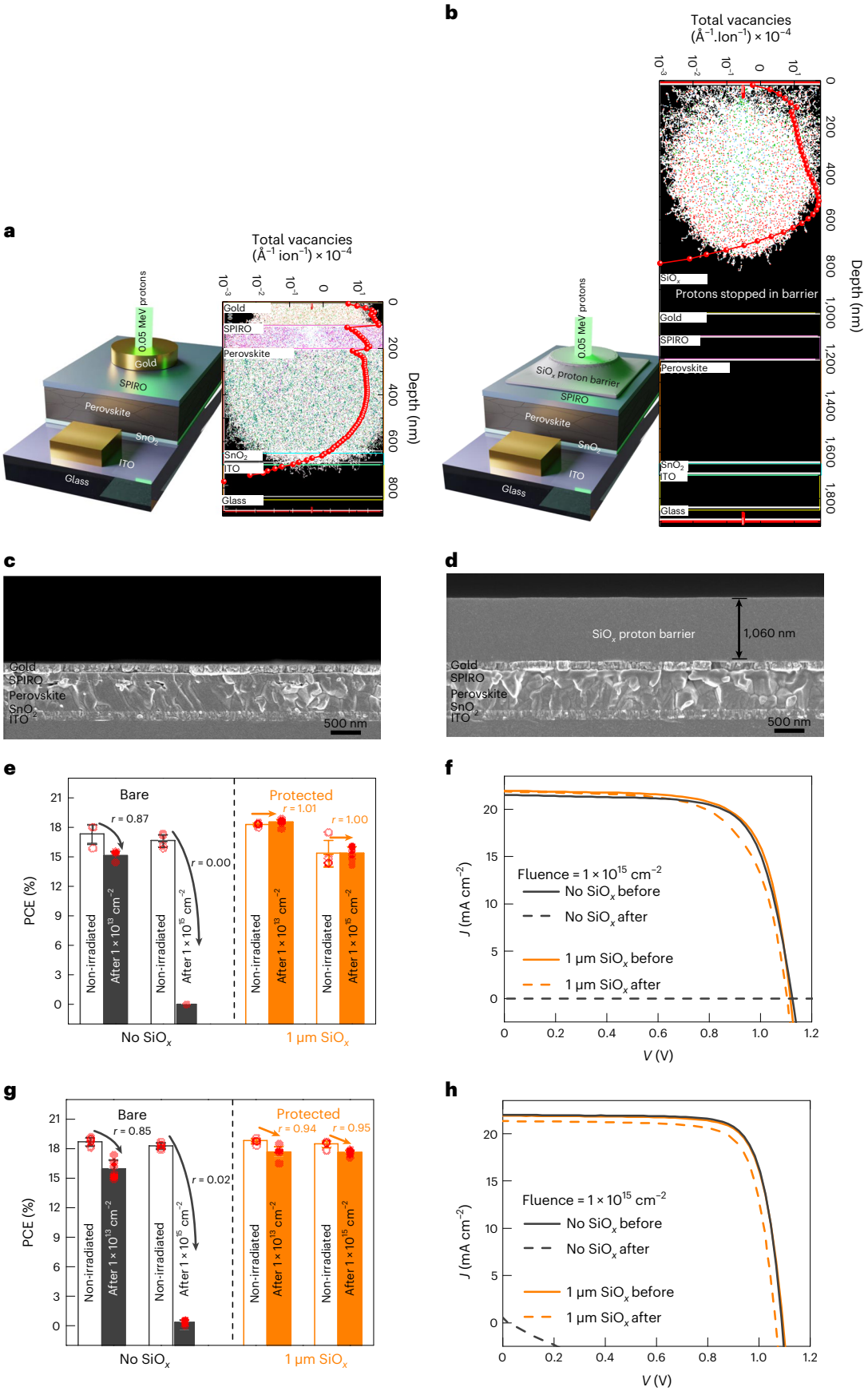

https://doi.org/10.1038/s41560-022-01189-1

Table 1 | Summary of device parameters and PCE remaining factors for n-i-p and p-i-n solar cells irradiated with 0.05 MeV protons at fluences of 10^{13} cm^{-2} and 10^{15} cm^{-2} with and without SiO_x proton barrier

Architecture	Proton fluence (cm^{-2})		Open circuit voltage (V)	Short circuit density ($mA\ cm^{-2}$)	Fill factor	PCE (%)	Remaining factor (PCE_{after}/PCE_{before})
n-i-p without SiO_x	10^{13}	Before	1.12±0	21.93±0.08	0.71±0.03	17.35±0.99	
		After	1.07±0	21.67±0.10	0.65±0.02	15.13±0.46	0.87±0.08
	10^{15}	Before	1.12±0.01	21.60±0.10	0.69±0.02	16.66±0.61	
		After	0	0	0	0	0
n-i-p with 1 µm SiO_x	10^{13}	Before	1.13±0	22.01±0.16	0.74±0	18.31±0.16	
		After	1.12±0	22.27±0.17	0.74±0.01	18.53±0.32	1.01±0.03
	10^{15}	Before	1.09±0.01	21.38±0.32	0.65±0.04	15.36±1.29	
		After	1.11±0.01	21.72±0.11	0.64±0.03	15.37±0.66	1.00±0.13
p-i-n without SiO_x	10^{13}	Before	1.09±0.01	21.98±0.17	0.78±0.01	18.70±0.39	
		After	1.05±0.01	20.18±0.45	0.75±0.01	15.95±0.87	0.85±0.06
	10^{15}	Before	1.09±0	22.01±0.07	0.76±0.01	18.30±0.28	
		After	0.42±0.27	3.00±1.86	0.18±0.02	0.33±0.25	0.02±0.01
p-i-n with 1 µm SiO_x	10^{13}	Before	1.09±0	21.92±0.10	0.78±0	18.82±0.25	
		After	1.08±0.01	21.35±0.17	0.76±0.02	17.65±0.64	0.94±0.05
	10^{15}	Before	1.09±0	21.84±0.19	0.77±0	18.49±0.29	
		After	1.07±0.01	21.29±0.07	0.77±0	17.61±0.26	0.95±0.03

These irradiation conditions (10^{-13} and 10^{-15} cm^{-2}) correspond to DDDs of 3.9×10^{-12} and 3.9×10^{-14} MeV g^{-1}, respectively. Each data point corresponds to averages over 3–6 devices. For sample size details, please see the source data. Error bars in the various device parameters correspond to the s.d.; error bars in the remaining factors correspond to the propagated error obtained after dividing the after- and before-irradiation device PCEs.

The effect of proton irradiation on the PCEs of perovskite solar cells with active surface areas of 0.1 cm^2 is shown in Fig. 1e,g, and representative *J*–*V* curves are shown in Fig. 1f,h. Devices without SiO_x are denoted 'bare' and those with SiO_x are labelled 'protected'. The ratio of the PCE of irradiated cell to the initial PCE before irradiation, the PCE remaining factor, is denoted as *r*. Bare solar cells lose ~15% of their initial PCEs when irradiated with a 10^{13} cm^{-2} fluence, 10^{15} cm^{-2} protons destroy these devices, reducing the efficiency to zero. The protected cells demonstrate a remarkable resilience to these fluences, in line with theoretical insights from the SRIM/TRIM simulations. All the 'protected' cells show a PCE remaining factor close to one. The benefit of SiO_x applies to any PV technology since the low-energy protons are blocked irrespective of the photoabsorber underneath. These ultrathin barriers can therefore be a transferable solution to space applications where high specific powers are desired.

The device parameters are summarized in Table 1. The PCE loss observed for the bare solar cells at 10^{13} cm^{-2} fluence is caused by a loss in each of the three parameters: open circuit voltage, short circuit density and fill factor. Nonetheless, a PCE remaining factor of 0.85 at such a high fluence is remarkable in comparison with conventional PV panels[31].

We sought to understand if this advantage offered by SiO_x extends to higher-energy protons as well. Higher-energy protons would not be blocked by 1 µm SiO_x given their longer range. However, we observed a higher remaining factor for solar cells capped with 1 µm SiO_x exposed to 1 MeV protons at a fluence of 10^{13} cm^{-2} (Supplementary Fig. 9). We discuss this unexpected finding below in the context of fully penetrating α-particle irradiation and proposed a barrier mechanism.

Supplementary Fig. 10 shows scanning electron microscopy (SEM) images for n-i-p solar cells with and without a SiO_x barrier irradiated with 0.05 MeV protons at a 10^{15} cm^{-2} fluence. A markedly distinct microstructure is visible in the bare device due to damage caused by the high proton fluence. External quantum efficiency (EQE) data are shown in Supplementary Fig. 11 and Supplementary Table 1 and confirm the short circuit density trends in Table 1. EQEs for the 10^{15} cm^{-2} irradiated cells are close to zero, as expected. For all the other devices, the EQEs remain almost unchanged. Encouraged by the proton-blocking capability of SiO_x, we sought to test its performance under other radiation stressors, such as atomic oxygen and α-irradiation.

Improved tolerance to atomic oxygen and α-particles

Atomic oxygen, α-particles and ultraviolet radiation are major stressors in the space environment[10]; however, thus far mostly untested in perovskite solar cells. We simulated the effect of atomic oxygen and ultraviolet irradiation by carrying out UVO treatment of the solar cells. During operation, a UVO chamber generates ultraviolet photons in the wavelength range of 200 nm, similar to the ultraviolet environment in LEO. On interaction with the atmospheric molecular oxygen in the chamber, these photons create atomic oxygen, which is responsible for ashing of the surface organics often used for cleaning. Figure 2a shows a normalized PCE of p-i-n triple-cation solar cells with and without an SiO_x barrier. The bare devices (16.3% PCE) underwent complete damage after 8 minutes of UVO exposure, whereas the protected devices retained their initial PCEs of 17.0% even after 20 minutes of exposure. Discolouration of a representative bare device is visible in the photographs shown on the top row of Fig. 2a. Atomic oxygen corrodes the silver electrodes as found by SEM. Figure 2d,f shows top-view SEM images of the metal electrode areas of the bare and protected cells, respectively. The bare cell (Fig. 2d) showed damage, which became obvious when the cross-section of this device was imaged (Fig. 2e). No noticeable changes were found for the protected device (Fig. 2f,g). After 30 minutes of exposure, a slight drop in PCE was observed for the cell with an SiO_x barrier. This performance reduction may be caused by a gradual erosion of SiO_x by atomic oxygen, which is visible as a whitish build-up atop the SiO_x layer in Fig. 2g. We note that the atomic oxygen flux experienced by the cells in the UVO chamber is probably several orders of magnitude higher compared with that of the LEO environment as atmospheric pressure on Earth and in the UVO chamber is 10^{11} times the pressure in the LEO. Therefore, the SiO_x layer is expected to undergo erosion in space at an extremely slow rate that is irrelevant to

https://doi.org/10.1038/s41560-022-01189-1

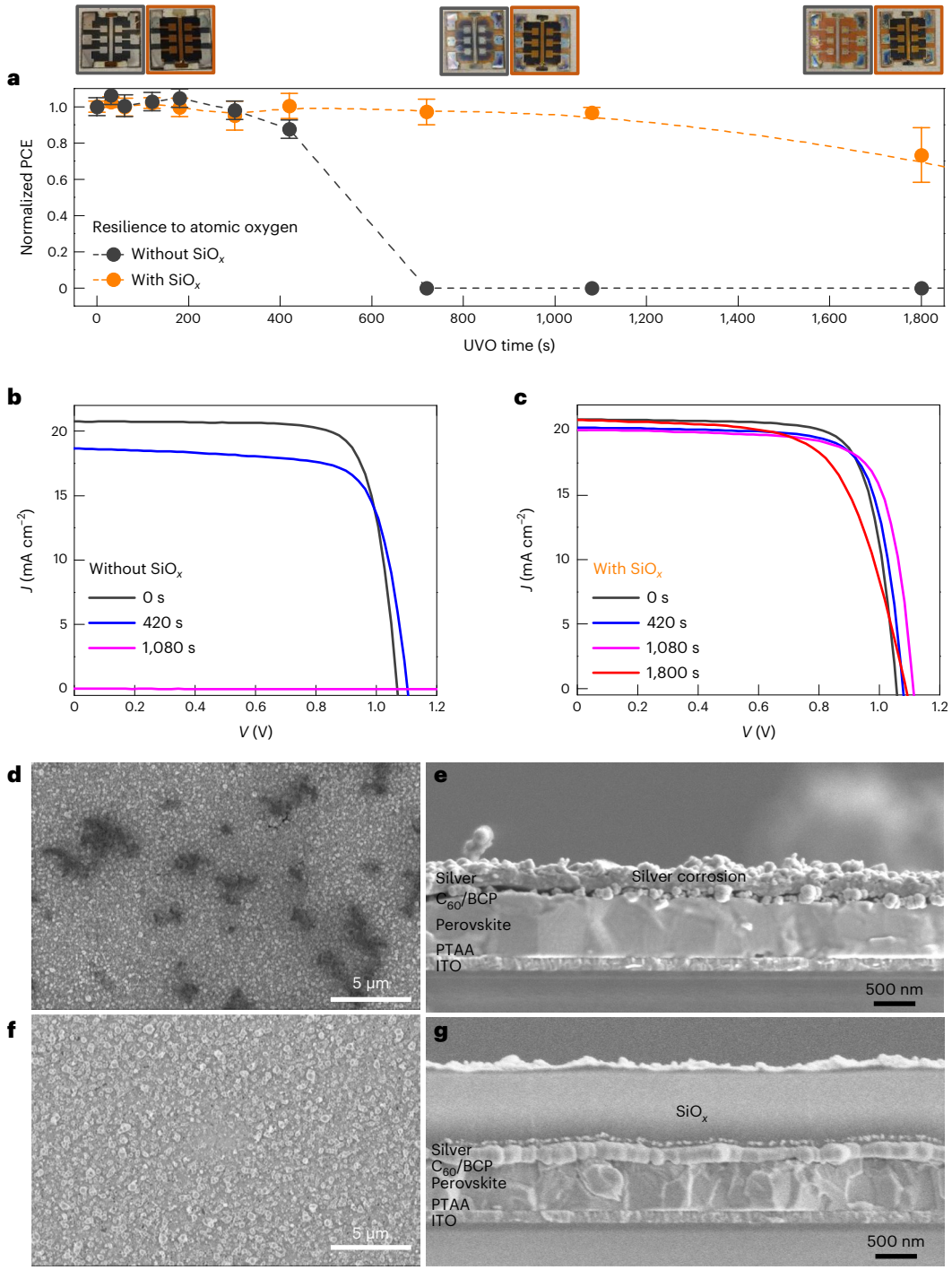

Fig. 2 | SiO*x* as an atomic oxygen barrier. a, p-i-n solar cells without (black) and with (orange) SiO_x exposed to atomic oxygen via UVO treatment. Each data point corresponds to an average over six devices. Error bars represent the propagated error obtained after dividing standard deviations in the exposed device PCEs by that in the initial device PCE. Photographs of the devices at exposure times of 0, 40 and 1,200 s are shown at the top. The initial PCEs for the devices without and with SiO_x were 16.6 ± 0.4 and 17.1 ± 0.3%, respectively. **b**,**c**, Corresponding *J*–*V* curves (forward scans) without (**b**) and with (**c**) SiO_x. **d**–**g**, Top-view (**d**,**f**) and X-SEM images (**e**,**g**) for UVO-treated devices without SiO_x (**d**,**e**) and with SiO_x (**f**,**g**).

the usual space mission durations of 5–15 years; therefore, these studies represent a worst case scenario under accelerated testing conditions.

Although α-particles are two orders of magnitude less abundant in space than protons, they are ~16 times more damaging and can pose a serious threat to space PV panels during solar particle events, such as solar storms[32]. Irradiation of p-i-n triple-cation solar cells with 2 MeV α-particles at a fluence of 2.0×10^{12} cm^{-2} from a Rutherford backscattering spectrometry set-up was then performed. SRIM/TRIM simulations (Supplementary Fig. 12a,b) confirmed that 1 μm is an insufficient thickness of SiO_x to stop α-particles of 2 MeV (as 2 MeV α-particles will penetrate ~8.5 μm in SiO_x). In fact, the simulations found these particles create an equal number of defects in the bare and SiO_x-capped solar cells. However, unexpectedly, the device with a 1 μm SiO_x barrier retained 99% of its initial PCE, whereas the bare solar cell lost ~50% of its initial PCE on irradiation (Supplementary Fig. 12c,d). To confirm this surprising observation, we repeated 2 MeV α-irradiation

on a different set of devices and irradiation was performed using an alternative α-source at a different institution. The repeat measurements confirmed that solar cells protected with 1 µm SiO_x retained their initial 18.0% PCEs after irradiation (Supplementary Fig. 12e,f).

Given the fully penetrating nature of 2 MeV α-particles, we used these experiments to estimate the lifetime of perovskites solar cells in various orbits of interest and to quantify the increase in lifetime from the SiO_x layer. Details of lifetime calculation are shown in Supplementary Figs. 14 and 15 and Supplementary Tables 2–4. Briefly, the cumulative annual displacement damage dose (DDD) in an orbit was calculated considering the proton fluence and non-ionizing energy loss (NIEL). NIEL is the energy that an incident proton deposits into a solar cell and causes non-ionizing atomic displacements and device degradation. The role of ionizing energy loss (IEL), incident proton's energy lost to electronic ionization, is still a topic of discussion in the context of perovskites and initial experiments suggest that it causes self-healing[6,33]. We therefore ignored the effect of IEL in this discussion by using low-energy protons for irradiation to minimize IEL. The ratio of IEL to NIEL is also low for α-particles due to their high mass (Supplementary Fig. 13). Protons were considered for cumulative DDD calculations as these are the primary source of displacement damage in space because of their higher fluence. Cumulative DDDs obtained for various orbits are shown in Supplementary Fig. 14 and highlight the role 1 µm SiO_x plays in reducing the radiation damage to solar cells. We found that the SiO_x layer remarkably increased the lifetime of perovskite solar cells in Earth's orbits and deep space. The lifetime in LEO (2,000 km altitude and 51° inclination) was increased from ~0.3 to ~6 years; a higher LEO was chosen here to provide an upper limit for the damage of perovskite cells with minimal protection in the LEO environments. For the orbit of Juno (Jupiter), the lifetime increased from ~1 to ~12 years. We also performed these calculations for the Tundra highly elliptical orbit, a high eccentricity orbit considered particularly important for space-based solar power[34]. We found that for this high-radiation environment, the SiO_x layer increased the device lifetime from ~0.3 to ~10 years (Supplementary Fig. 15). Orbit parameters considered for these calculations are provided in Methods. Lifetime calculations are explained in Supplementary Note 1.

Resilience to fully penetrating α-particles is a promising finding and suggests that an incident particle, such as a higher-energy proton, is not required to be fully blocked in the SiO_x layer to limit damage to the device. Although a full analysis of this unexpected observation will involve a detailed interfacial diagnosis of the irradiated solar cell and is beyond the scope of this work, a possible explanation is presented. We postulate that the SiO_x layer acts as a chemical barrier to any component of the perovskite lattice that is dislodged on irradiation and blocks its escape, and thereby preserves the stoichiometry and out diffusion of the lighter elements. In fact, the organic A-site cation has a higher probability of being knocked off given its volatility, as highlighted recently for perovskite solar cells that operate under vacuum[35]. In the following sections, evidence is provided in favour of this possibility by demonstrating that SiO_x indeed serves as a chemical barrier.

Improved tolerance to polar solvents

The above demonstrations establish that SiO_x hardens perovskite solar cells against protons, α-particles and atomic oxygen. We were interested in exploring if SiO_x barrier layers have a broader scope beyond space applications. Targeting terrestrial compatibility, the tolerance of the SiO_x-protected cells was tested against polar solvents. Figure 3 shows the effect of deionized water submergence on the performance of p-i-n triple-cation and $CsPbI_2Br$ cells. Although the direct interaction of solar panels with water is not a realistic scenario, such a test takes the moisture tolerance aspect to the extreme. Here again, we found that SiO_x-capped p-i-n triple-cation and $CsPbI_2Br$ cells retain ~90% of their initial PCEs (15.0% and 11.9%, respectively) after one minute of deionized water dipping. The case of the $CsPbI_2Br$ device is particularly remarkable given its intrinsic intolerance to moisture[36,37]. In fact, the bare $CsPbI_2Br$ device denoted by the dashed black curve in Fig. 3b with an initial PCE of 11.7% was completely damaged on contact with water, whereas the protected cell retained its brown colour and performance. Supplementary Videos 1 and 2 show this experiment. SEM images in Fig. 3c,d illustrate the extent of damage on the p-i-n triple-cation cell on water dipping. The SiO_x barrier blocks any interaction of the cell with water and leaves it undamaged (Fig. 3e,f).

The design of such experiments is complicated because the substrate edges and the electrode area that are contacted for the *J*–*V* measurements provide ingress pathways to solvent molecules, which can travel laterally and damage the cell. However, the fact that polar solvents are not able to immediately attack and damage the SiO_x-capped cells suggests that a direct impact of solvents with the cells is blocked. We expect a packaging strategy that combines SiO_x with edge sealing to result in longer submergence times.

We also performed a similar dipping experiment with the polar solvent DMF. As most of the perovskite ink formulations, in general, are based on DMF, the solvent is expected to completely dissolve the perovskite layer on contact. DMF dipping is therefore one of the harshest tests to quantify the resilience of a barrier layer technology for perovskites. Although the cells dipped in DMF suffered performance losses, the active layer of the bare cells immediately dissolved on contact with DMF, but the SiO_x-capped devices retained their dark appearance (Supplementary Videos 3–5).

It is important to highlight the damage that ultraviolet radiation, atomic oxygen and deionized water inflict on the perovskite covered by the metal electrode, as shown in the device photographs in Figs. 2a and 3d. This damage, evidenced by the loss of the dark brown colour, suggests that the 100-nm-thick metal electrode is not sufficient to protect the cell stack underneath from radiation and deionized water. Although deionized water can still enter through the edges and travel laterally towards the device stack, it is clear that ultraviolet photons and atomic oxygen go through the metal electrode and destroy the perovskite due to their normal incidence. This implies that larger area solar cells and modules with a fully metallized rear surface will also suffer from this degradation due to the permeability of the metal surface. Additionally, fully metallized modules also have laser patterning and the resulting scribe lines will act as ingress pathways. Although increasing the thickness of the rear metal to ~300 nm can block low-energy protons (Supplementary Fig. 16) and address the deionized water permeability issues of a thinner metal electrode, ultraviolet radiation and atomic oxygen will still corrode silver over time. Also, this does not address the solvent ingress that will happen via the laser scribe lines, which will still have to be infilled with an electrically insulating layer such as SiO_x.

Improved shelf life of moisture-sensitive Sn-Pb and $CsPbI_2Br$ cells

The remarkable morphological uniformity of the SiO_x layer, as evidenced by SEM, also points towards its potential as a moisture and chemical barrier for terrestrial applications. To illustrate this point, we chose two perovskite absorber chemistries that are highly sensitive to moisture. Solar cells based on the low bandgap (1.25 eV) Sn–Pb absorber are usually characterized inside a N_2 glove box as exposing them to the ambient without encapsulation results in degradation[22]. Similarly, solar cells based on the wide bandgap (1.88 eV) $CsPbI_2Br$ perovskite absorbers are sensitive to moisture[36]. Although, these chemistries are very promising for tandem solar cell designs, their moisture sensitivity needs to be addressed for industrial implementation. As such, these chemistries present a litmus test for the barrier properties of SiO_x. Figure 4a shows PCEs of Sn–Pb solar cells measured in the ambient. As expected, bare cells without SiO_x immediately degraded (black bars) and lost almost all of their initial PCEs within four minutes. However, the SiO_x-capped cells fully retained their initial PCEs (15.6%), that is, were stable in the ambient. To the best of our knowledge, this is the

https://doi.org/10.1038/s41560-022-01189-1

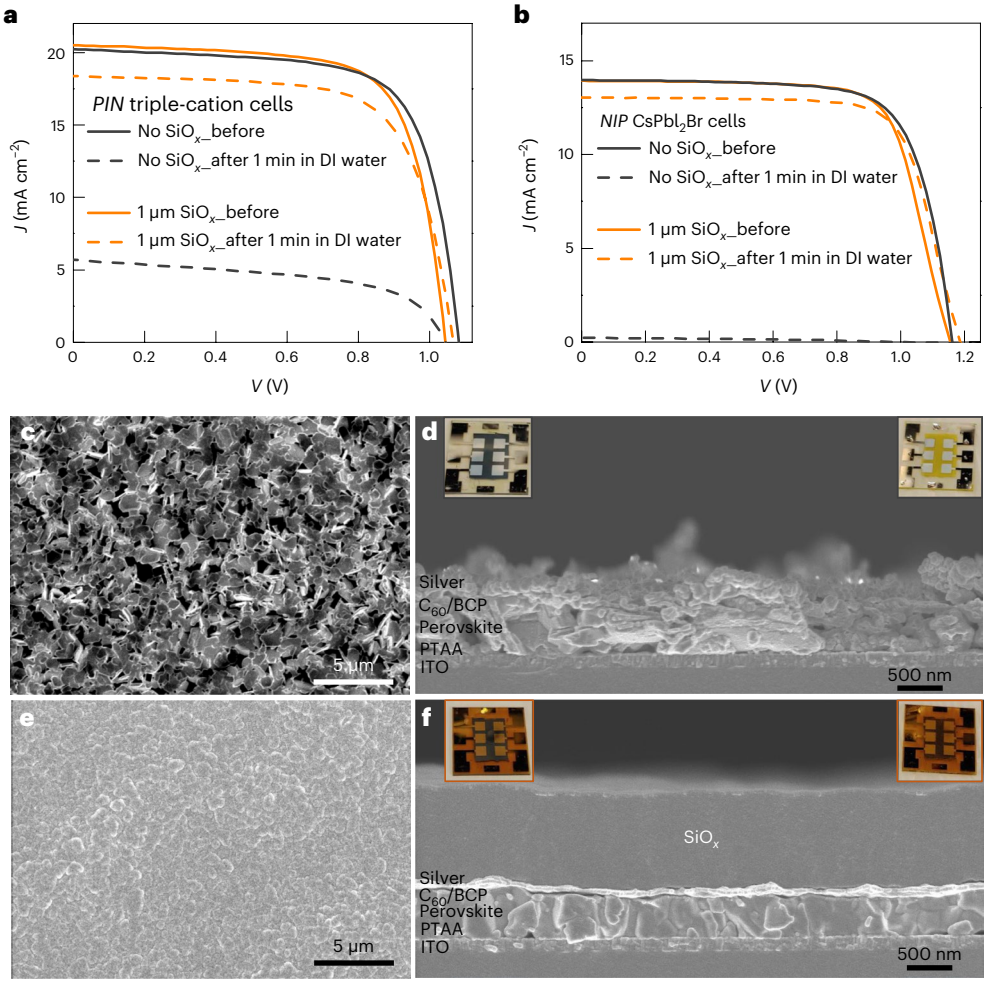

Fig. 3 | SiO*x* as water barrier. a, *J*–*V* curves (forward scans) for p-i-n triple cation devices without (black) and with (orange) SiO_x before (solid) and after (dashed) 1 min of dipping in deionized water. **b**, Similar experiments performed for $CsPbI_2Br$ cells (reverse scans). **c**,**d**, Top-view (**c**) and X-SEM images (**d**) of the water-dipped p-i-n device without SiO_x **e**,**f**, Top view (**e**) and X-SEM images (**f**) of the water-dipped p-i-n device with SiO_x. Insets: photographs of the cells before (left) and after (right) water dipping.

first instance when Sn–Pb solar cells have been measured in ambient and found to be stable, retaining 100% of their PCE. Previous reports carried out *J*–*V* testing either in a N_2 environment, or a glass–glass encapsulation was used to measure these cells in the ambient[22,38,39]. SiO_x was similarly found to enhance the ambient shelf life of $CsPbI_2Br$ solar cells (Fig. 4c) with the protected cells retaining their initial PCE of ~12.0% even after 100 days in the ambient. The bare cells underwent phase segregation and turned transparent within only a few days in the ambient. These observations confirm that the SiO_x layer suppressed moisture ingress and prolonged the shelf life.

Promising barrier strategies demonstrated for perovskite solar cells mostly rely on deposition techniques that may be challenging to implement at the industrial scale[14,18,40,41]. Further, it was reported that some barrier layers could cause as much as a 30% drop in the device performance, pointing towards an undesirable chemical interaction of the barrier layer with the device stack underneath[42,43]. Overall, these earlier reports only focused on improving moisture resilience, whereas tolerance against space stressors, such as proton, ultraviolet and α-radiation and atomic oxygen, was not explored. The SiO_x barrier layer presented here overcomes the industrial scale-up challenges mentioned above by relying on thermal evaporation, and concomitantly hardens the perovskite solar cells against well-known space and terrestrial stressors. Additionally, although deposition rates of atomic layer deposition barriers were limited to 0.4–0.8 nm min^{-1} in earlier reports, the SiO_x barriers demonstrated here achieve a ×30 higher deposition rate of ~25 nm min^{-1}. Depositing the barrier atop a finished perovskite solar cell also allows one to decouple it from charge transport within the device. In cases where barriers are part of the device stack, care must be taken to ensure efficient charge transport across them, and such a stack may still require additional protection atop the finished device[17]. We identified multiple requirements to grow efficient barriers atop perovskite solar cells. The barrier layer should be: (1) low cost, (2) amenable to thermal evaporation at high deposition rates, (3) mechanically robust without crazing or peel off, (4) electrically insulating to avoid pixel cross-talk, (5) chemically non-interactive with the perovskite device stack underneath, (6) insoluble in most polar and non-polar solvents and (7) optimally thick to improve the terrestrial and space tolerance without compromising specific power. The remarkable benefits and technological potential of the SiO_x barrier demonstrated in this report are such since it meets all these specifications.

It is important that all the above-mentioned criteria be simultaneously met by a potential barrier layer technology. We explored alternatives by depositing MoO_x and indium tin oxide (ITO) barriers. Both layers can theoretically block low-energy protons within thicknesses of a few hundred nanometres. A ~650 nm MoO_x layer thermally deposited directly atop perovskite solar cells was found to be mechanically

https://doi.org/10.1038/s41560-022-01189-1

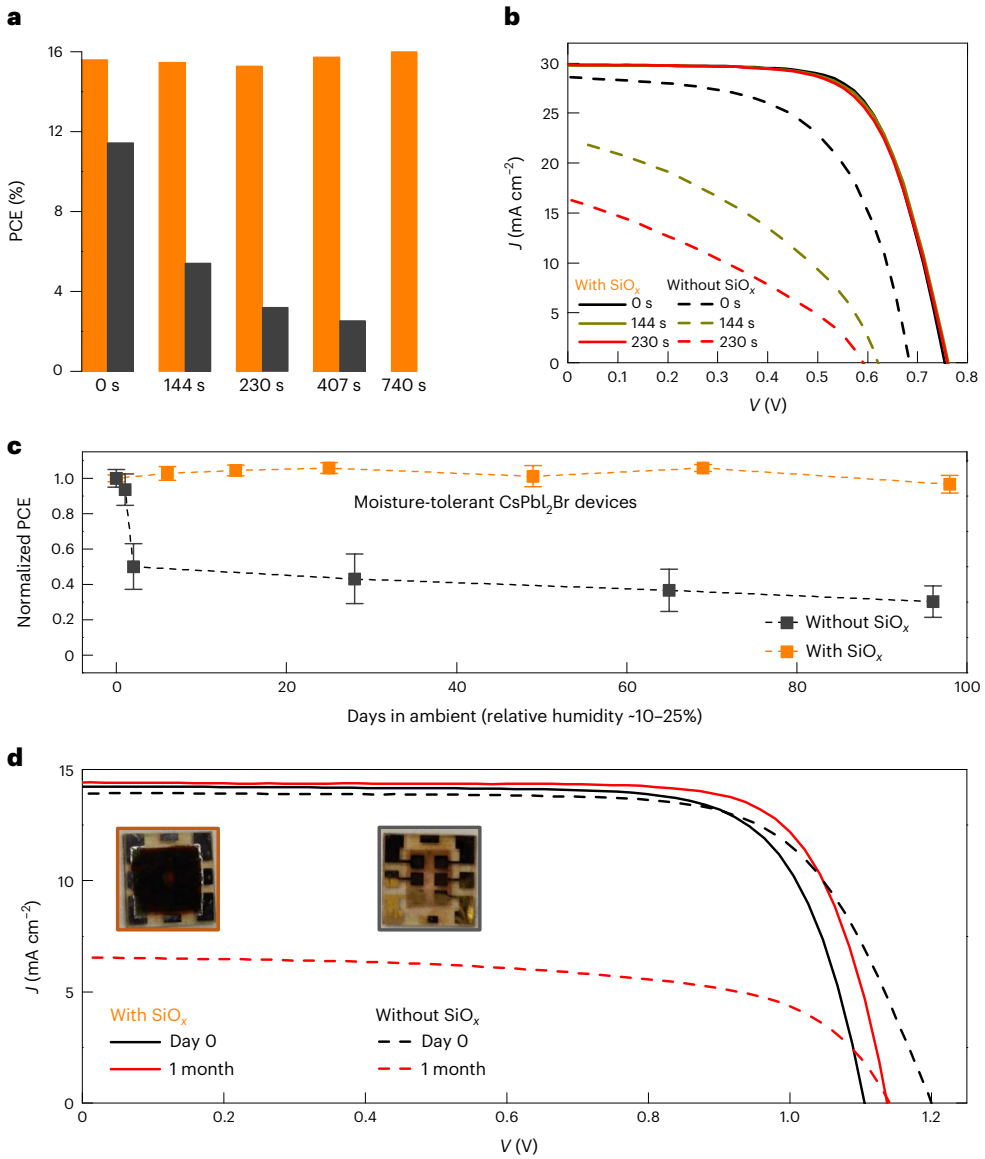

Fig. 4 | SiO*x* as a moisture barrier for sensitive chemistries. a, Bar graphs showing the PCEs of Sn–Pb devices measured in the ambient without (black) and with (orange) SiO_x for various ambient exposure times. **b**, Corresponding *J*–*V* curves (reverse scans), where dashed curves correspond to the devices without SiO_x and the solid ones to those with SiO_x. **c**, Shelf life of all-inorganic $CsPbI_2Br$ devices stored in the ambient. Each data point corresponds to the average over five devices. The error bars represent the propagated error obtained after dividing standard deviations in the aged device PCEs by that in the initial device PCE. Initial PCEs for the $CsPbI_2Br$ devices without and with SiO_x are 11.5 ± 0.4% and 11.7 ± 0.2%, respectively. **d**, Corresponding *J*–*V* curves (reverse scans) of representative devices at the start of ambient ageing (black) and after 1 month (red).

unstable and peeled off immediately after deposition. Initially, 20.1% PCE p-i-n triple cation solar cells completely degraded (to 0% PCE) after deposition. The few solar cells in which MoO_x remained intact were found to have a severely reduced PCE of 7% (Supplementary Fig. 17). This is likely to point towards an undesirable interaction of the MoO_x film with the device stack underneath. For the ITO barrier deposition, sheet resistance (~10,000 $\Omega\,\square^{-1}$) was increased by carrying out sputtering in an oxygen-rich atmosphere. Owing to time limitations, a ~300 nm ITO layer was deposited atop the devices. A marginal drop in PCEs from 20.2 to 19.4% was found after the ITO deposition. The devices retained ~93% of their initial PCEs after irradiation with 0.05 MeV protons of 10^{13} cm^{-2} fluence. Although ITO exhibited excellent stability against mechanical peel off, high-resolution SEM showed highly irregular but conformal coating (Supplementary Fig. 18), which may be the cause of the reduction in fill factor and subsequent device performance reduction on deposition. Chemical interaction within the layers may also reduce the performance of the device. These experiments highlight the uniqueness of SiO_x barriers. It is likely that these challenges associated with the MoO_x and ITO barriers could be addressed; however, SiO_x shown here works well and does not appear to suffer from these issues.

Finally, we extended the theoretical analysis to a library of other metal oxide barriers: Al_2O_3, ZrO_2 and HfO_2. These have higher mass densities than that of SiO_x (2.13 g cm^{-3}) and are therefore expected to behave as better proton stoppers due to an increased interaction with the incident protons. All of these layers efficiently block protons from entering the perovskite device stack, as found from the SRIM/TRIM simulations shown in Supplementary Fig. 19. Indeed, Al_2O_3, ZrO_2 and HfO_2 are found to be more efficient proton barriers owing to a lower proton stopping range of ~330 nm than that of SiO_x (~550 nm). These layers can be deposited via atomic layer deposition or electron beam and are summarized in Supplementary Table 5.

Conclusions

In summary, we have demonstrated a low-cost barrier technology based on ultralightweight metal oxide layers that can be feasibly deposited on perovskite solar cells. Devices capped with 1-µm-thick SiO_x layers showed a surprising resilience to harmful protons at ultrahigh fluences of 10^{15} cm^{-2}, and also impart tolerance against ultraviolet radiation, atomic oxygen and α-irradiation. The proposed technology cuts down the solar array encapsulation weight by >99% compared with that of conventional radiation barriers, which involve ~150-µm-thick cover glass and elastomer encapsulants. The oxide layer also acts as a moisture and chemical barrier, which bolsters the shelf life and makes cells resilient under polar solvents, with immediate implications for terrestrial applications.

Methods

Materials

PbI_2 (99.99%) and $PbBr_2$ (>98.0%) were purchased from TCI America. Formamidinium iodide and methylammonium bromide were purchased from GreatCell Solar Materials. Li-TFSI (bis(trifluoromethane) sulfonimide lithium salt) was purchased from Alfa Aesar. CsI (99.999%) and 4-*tert*-butylpyridine (96%) were purchased from Sigma Aldrich. SPIRO (2,2′,7,7′-tetrakis(*N*,*N*-di-*p*-methoxyphenylamino)−9,9′-spiro bifluorene) (≥99.5%) was purchased from Lumtec, PTAA (poly(triaryl amine)) (5–20 kDa) was obtained from Solaris Chem, PFN-Br (poly(-9,9-bis(3′-(*N*,*N*-dimethyl)-*N*-ethylammoinium-propyl-2,7-fluorene)-alt-2,7-(9,9-dioctylfluorene))dibromide) was purchased from 1-Material. The SnO_2 colloidal dispersion was obtained from Alfa Aesar and diluted to 1.5% in deionized water before use. C_{60}, bathocpurine (BCP) and all the solvents (DMF, dimethylsulfoxide (DMSO), chlorobenzene, toluene, methanol and methyl acetate) were obtained from Sigma Aldrich. SnI_2 (99.99% trace metals basis) and SnF_2 were purchased from Sigma-Aldrich. SiO_x granules were purchased from RD Mathis (SIO39X24, 99.9% silicon monoxide granules, 2–4 mm).

Triple-cation perovskite active layer fabrication

This procedure was common to both the n-i-p and p-i-n devices and was done in a N_2 glove box. PbI_2 (507 mg), $PbBr_2$ (73.4 mg), methylammonium bromide (22.4 mg), formamidinium iodide (172 mg) and CsI (15.6 mg) precursors were mixed in 1 ml of a DMF/DMSO solvent mixture (4:1 v/v) and vortexed to form a 1.26 M ink. The ink was filtered using a 0.45 mm nylon filter. The ink (50 µl) was dropped on the ITO/quartz substrate and spun at 1,000 r.p.m. for 10 s followed by 6,000 r.p.m. for 20 s. Chlorobenzene (150 µl) was dropped in a continuous stream at the spinning substrates with 5 s remaining at the end of the spin cycle. This antisolvent rinse step changed the appearance of the spinning film from transparent to a mild orange. After completion of the spin cycle, the substrate was immediately placed on a hotplate set at 100 °C for 60 min. Within seconds of contact with the hotplate, the film converted into the black perovskite phase.

$CsPbI_2Br$ perovskite active layer fabrication

This procedure was done in a N_2 glove box. CsI (312 mg), $PbBr_2$ (220 mg) and PbI_2 (277 mg) precursors were mixed in 1 ml of DMSO and vortexed to form a 1.2 M ink. The ink was filtered using a 0.45 mm nylon filter, and then 50 µl of the ink dropped on the substrate was spun at 1,500 r.p.m. for 15 s followed by 4,500 r.p.m. for 45 s. Methyl acetate (150 µl) was dropped in a continuous stream at the spinning substrates with 15 s remaining at the end of the spin cycle. After completion of the spin cycle, the substrate was immediately placed on a hotplate set at 135 °C for 1 min. Within seconds of contact with the hot plate, the film converted into the dark brown perovskite phase.

Sn–Pb perovskite active layer fabrication

The pre-patterned ITO substrates were sequentially cleaned ultrasonically in acetone and isopropanol for 30 min. PEDOT:PSS (poly(3,4-ethylenedioxythiophene) polystyrene sulfonate) was spin coated onto the ITO substrate at 3,000 r.p.m. and annealed at 150 °C for 20 min in air. To make the narrow bandgap $(FASnI_3)_{0.6}(MAPbI_3)_{0.4}$ precursor, formamidinium iodide (0.6 mmol), SnI_2 (0.6 mmol), SnF_2 (0.06 mmol), MAI (0.4 mmol) and PbI_2 (0.4 mmol) were mixed in 600 µl of DMF/DMSO (4:1 v/v) in a N_2 glove box. The $(FASnI_3)_{0.6}(MAPbI_3)_{0.4}$-based precursors were spin coated onto the ITO/PEDOT:PSS substrates in the glove box at 5,000 r.p.m. for 30 s and 350 µl of toluene was dripped onto the spinning substrate. The resulting perovskite films were then thermally annealed at 100 °C for 10 min. Finally, 30 nm C_{60}, 6 nm BCP and 100 nm Ag were sequentially thermally evaporated on the perovskite layer.

Device fabrication

Quartz substrates (Ted Pella) with dimensions of 25.4 mm × 25.4 mm × 1 mm with 150 nm ITO deposited in-house (sheet resistance ~15 $\Omega\,\square^{-1}$) were cleaned by sequential sonication in acetone (15 min) and isopropanol (15 min) purchased from Sigma Aldrich. Substrates were blow-dried with nitrogen followed by 10 min of UVO treatment.

For n-i-p triple-cation and $CsPbI_2Br$ devices, 150 µl of SnO_2 colloid was dropped on each substrate followed by spin coating at 3,000 r.p.m. for 15 s. The coated substrates were placed on a hotplate set at 150 °C for 30 min. This was followed by a further 10 min of UVO treatment after which the substrates were transferred to a N_2 glove box in which the perovskite active layer fabrication was completed as described above. spiro-OMeTAD (2,2′,7,7′-tetrakis(*N*,*N*-di-*p*-methoxyphenyl-amine 9,9′-spirobifluorene) was next deposited by dynamically spinning 10 µl of spiro-OMeTAD solution at 5,000 r.p.m. for 15 s. This solution was made immediately before deposition by dissolving 36.1 mg of spiro-OMeTAD, 14.4 µl of 4-*tert*-butylpyridine and 8.8 µl of Li-TFSI salt (520 mg in 1 ml of acetonitrile) in 0.5 ml of chlorobenzene.

For p-i-n triple-cation devices, the UVO-cleaned substrates were immediately transferred to the N_2 glove box for PTAA deposition. PTAA solution (50 µl, 2 mg ml^{-1} in toluene) was spin coated at 6,000 r.p.m. for 30 s. The coated substrate was placed on a hotplate set at 100 °C for 10 min. This was followed by dynamic spinning of 50 µl of PFN-Br solution (0.5 mg ml^{-1} in methanol) at 5,000 r.p.m. for 30 s. The perovskite active layer was next deposited, as detailed above.

Thermal evaporation

For n-i-p triple-cation and $CsPbI_2Br$ devices, 100 nm of gold was evaporated using a shadow mask at 0.5 Å s^{-1} for the first 10 nm and 2.0 Å s^{-1} for the remaining 90 nm. For p-i-n triple-cation devices, 25 nm C_{60} (0.30 Å s^{-1}), 6 nm BCP (0.15 Å s^{-1}) and 100 nm silver (0.5 Å s^{-1} for the first 10 nm and 2.0 Å s^{-1} for the remaining 90 nm) were deposited.

For SiO_x-capped cells, 1,000 nm of SiO_x was evaporated on the device stack at 0.5 Å s^{-1} for the first 10 nm, 2.0 Å s^{-1} for the next 100 nm and 5.0 Å s^{-1} for the remaining 890 nm. Evaporation was carried out at a base pressure of 10^{-7} torr. Solar cells were held at room temperature and the substrate holder was actively cooled with water to avoid heating of the solar cells during evaporation. No oxygen was used during the evaporation.

ITO barrier deposition

The ITO (90% tin oxide, 10% indium oxide from Plasmaterials) was sputtered using a 13.56 MHz radiofrequency source (~0.3 W cm^{-2}) using 10 sccm Ar and 0.5% O_2 at 30 mtorr at room temperature.

J–*V* characterization

Solar cells were measured at room temperature in a N_2 glove box with a source meter (Keithley 2420) using a solar simulator (Newport, Oriel Class AAA, 94063A) at a 100 mW cm^{-2} illumination (AM 1.5 G). Light illumination was done from the glass substrate side. The simulator was calibrated using an NREL-calibrated Si photodiode. The spectral mismatch between the reference and perovskite devices was calculated

using a KG2 filter. The devices were measured at room temperature in a N_2 glove box in reverse scan (1.4 to −0.2 V) and forward scan (−0.2 to 1.4 V) modes at a scan speed of 0.464 V s^{-1} and step size of 0.02 V. The device area was 0.1 cm^2 and the active area was defined by a metal aperture (0.058 cm^2). Sn–Pb perovskite solar cells were tested in ambient (room temperature and relative humidity of ~20–25%).

A separate solar cell was considered for each irradiation condition, and the *J*–*V* data were taken before and after irradiation. There was an average time gap of one week between the before and after *J*–*V* measurements due to the overall time required to ship the samples to the radiation facility (University of North Texas (UNT)), the irradiation runs and to ship the samples back to NREL for testing.

SEM characterization

SEM imaging was performed on a Hitachi 4800 field emission electron microscope. Samples were mounted with carbon paint, and imaging was executed at a working distance range of 5–8 mm, as recommended by the vendor. Owing to the volatility of the perovskites, conservative imaging parameters were utilized, with lower energy and lower current settings. In the cross-sectional orientation, a thin layer of gold was applied to mitigate charging effects.

SPENVIS calculations

Proton fluences for various orbits were simulated using SPENVIS. AP-8 and AE-8 models were used for Earth orbits, whereas the D&G83 model was used for the Juno orbit. GEO orbit parameters are built into SPENVIS; the following parameters were used for the other orbits discussed:

- International Space Station orbit: perigee altitude = 417 km, apogee altitude = 422 km, inclination = 51.64°, argument of perigee = 42.17°, true anomaly = 130.61°.
- LEO (circular orbit): altitude = 2,000 km, inclination = 51.0°.
- 5,000 km (circular orbit): altitude = 5,000 km, inclination = 60.0°.
- Juno: perijove altitude = 75,600 km, apojove altitude = 8,100,000 km, inclination = 90°.
- Tundra orbit: semi-major axis = 46,000 km, eccentricity = 0.4, inclination = 63.4°, longitude of apogee = 90°, argument of perigee = 270°, true anomaly = 130.61°.

SRIM simulations

SRIM simulations were performed considering 100,000 protons using the 'full damage cascade' calculation mode. The following device structures were considered:

- n-i-p device without SiO_x: Au (100 nm)/SPIRO (100 nm)/$Cs_{0.05}(MA_{0.17}FA_{0.83})_{0.95}Pb(I_{0.83}Br_{0.17})_3$ (450 nm)/SnO_2 (50 nm)/ITO (150 nm)/glass (70 nm).
- n-i-p device with SiO_x: SiO_x (1,000 nm)/Au (100 nm)/SPIRO (100 nm)/$Cs_{0.05}(MA_{0.17}FA_{0.83})_{0.95}Pb(I_{0.83}Br_{0.17})_3$ (450 nm)/SnO_2 (50 nm)/ITO (150 nm)/glass (70 nm).
- p-i-n device without SiO_x: Ag (100 nm)/BCP (6 nm)/C_{60} (25 nm)/$Cs_{0.05}(MA_{0.17}FA_{0.83})_{0.95}Pb(I_{0.83}Br_{0.17})_3$ (450 nm)/PTAA (5 nm)/ITO (150 nm)/glass (70 nm).
- p-i-n device with SiO_x: SiO_x (1,000 nm)/Ag (100 nm)/BCP (6 nm)/C_{60} (25 nm)/$Cs_{0.05}(MA_{0.17}FA_{0.83})_{0.95}Pb(I_{0.83}Br_{0.17})_3$ (450 nm)/PTAA (5 nm)/ITO (150 nm)/glass (70 nm).

Protons were irradiated from the metal electrode side. A low glass substrate thickness was considered to speed up the calculations.

The mass densities used were SiO_x = 2.13 g cm^{-3}, Al_2O_3 = 3.95 g cm^{-3}, ZrO_2 = 5.68 g cm^{-3}, HfO_2 = 9.68 g cm^{-3}, Au = 19.31 g cm^{-3}, SPIRO = 1.40 g cm^{-3}, PTAA = 1.40 g cm^{-3}, C_{60} = 1.65 g cm^{-3}, BCP = 1.2 g cm^{-3}, $Cs_{0.05}(MA_{0.17}FA_{0.83})_{0.95}Pb(I_{0.83}Br_{0.17})_3$ = 4.32 g cm^{-3}, SnO_2 = 6.95 g cm^{-3}, ITO = 7.20 g cm^{-3} and glass = 2.53 g cm^{-3}.

The displacement energies used were Au = 25 eV, C = 28 eV, H = 10 eV, N = 28 eV, O = 28 eV, Cs = 25 eV, Pb = 25 eV, I = 25 eV, Br = 25 eV, Si = 15 eV, In = 25 eV, Sn = 25 eV, Al = 25 eV, Zr = 25 eV and Hf = 25 eV.

Proton and α-irradiation at UNT

Proton irradiation was performed at the UNT Ion Beam Laboratory. The 50 keV proton beams were extracted from a TiH solid cathode with SNICS-II (Source of Negative Ions by Cesium Sputtering, NEC) associated with a 3 MV tandem accelerator (NEC 9SDH-2)[44]. The momentum-analysed proton beams were electrostatically raster scanned over the samples for uniform irradiation in a low-energy irradiation facility before they were injected into the tandem accelerator. The samples received either a 1.0×10^{13} or 1.0×10^{15} protons cm^{-2} fluence. The proton flux was kept to similar levels that did not result in spatial variation or substantial heating of the different target materials. All the samples received a flux of 3.125×10^{11} protons cm^{-2} s^{-1}. The ion implantation occurred under a vacuum of 1×10^{-7} torr. The 2 MeV α-irradiation was performed using He ion beams produced using a single-ended pelletron accelerator (NEC-9SDH) with a radiofrequency ion source[45]. The beam flux was 9.375×10^{10} particles cm^{-2} s^{-1}.

α-irradiation at NREL

The accelerated helium ion source used was a model 3S-MR10 Rutherford backscattering spectrometry system from the NEC located at NREL. To enable the tuning of fluences down to 2.0×10^{12} cm^{-2}, the beam current was turned down, relative to those commonly used for Rutherford backscattering spectrometry measurements, to 1 nA for irradiation at 2 MeV. The charge accumulation for dosing was set to 0.01 and 0.1 μC to obtain fluences of 2.0×10^{12} and 2×10^{13} cm^{-2}, respectively.

Reporting summary

Further information on research design is available in the Nature Portfolio Reporting Summary linked to this article.

Data availability

All of the data generated or analysed during this study are included in the published article and its Supplementary Information files. Source data are provided with this paper.

References

1. Ho-Baillie, A. W. Y. et al. Deployment opportunities for space photovoltaics and the prospects for perovskite solar cells. *Adv. Mater. Technol.* **7**, 2101059 (2021).
2. Akyildiz, I. F. & Kak, A. The Internet of Space Things/CubeSats. *IEEE Netw.* **33**, 212–218 (2019).
3. Sasaki, S., Tanaka, K. & Maki, K. Microwave power transmission technologies for solar power satellites. *Proc. IEEE* **101**, 1438–1447 (2013).
4. Abiri, B. et al. A lightweight space-based solar power generation and transmission satellite. Preprint at https://doi.org/10.48550/arXiv.2206.08373 (2022).
5. Luo, P. et al. Correlation between structural evolution and device performance of $CH_3NH_3PbI_3$ solar cells under proton irradiation. *ACS Appl. Energy Mater.* **4**, 13504–13515 (2021).
6. Durant, B. K. et al. Tolerance of perovskite solar cells to targeted proton irradiation and electronic ionization induced healing. *ACS Energy Lett.* **6**, 2362–2368 (2021).
7. Yang, J., Bao, Q., Shen, L. & Ding, L. Potential applications for perovskite solar cells in space. *Nano Energy* **76**, 105019 (2020).
8. Curtin, D. J. & Statler, R. L. Review of radiation damage to silicon solar cells. *IEEE Trans. Aerosp. Electron. Syst.* **AES-11**, 499–513 (1975).
9. Lang, F. et al. Proton-radiation tolerant all-perovskite multijunction solar cells. *Adv. Energy Mater.* **11**, 2102246 (2021).

10. Tu, Y. et al. Perovskite solar cells for space applications: progress and challenges. *Adv. Mater.* https://doi.org/10.1002/adma.202006545 (2021).
11. Huang, J.-S. et al. in *2017 IEEE 44th Photovoltaic Specialist Conference (PVSC)* 1248–1252 (IEEE, 2017).
12. Miyazawa, Y. et al. Tolerance of perovskite solar cell to high-energy particle irradiations in space environment. *iScience* **2**, 148–155 (2018).
13. Statler, R. L. & Curtin, D. J. Radiation damage in silicon solar cells from low-energy protons. *IEEE Trans. Electron Devices* **18**, 412–417 (1971).
14. Hosseinian Ahangharnejhad, R. et al. Protecting perovskite solar cells against moisture-induced degradation with sputtered inorganic barrier layers. *ACS Appl. Energy Mater.* **4**, 7571–7578 (2021).
15. Choi, E. Y. et al. Enhancing stability for organic–inorganic perovskite solar cells by atomic layer deposited Al_2O_3 encapsulation. *Sol. Energy Mater. Sol. Cells* **188**, 37–45 (2018).
16. Kim, H. et al. Enhanced stability of $MAPbI_3$ perovskite solar cells using poly(*p*-chloro-xylylene) encapsulation. *Sci. Rep.* **9**, 15461 (2019).
17. Zhao, Y. et al. A bilayer conducting polymer structure for planar perovskite solar cells with over 1,400 hours operational stability at elevated temperatures. *Nat. Energy* **7**, 144–152 (2022).
18. McKenna, B., Troughton, J. R., Watson, T. M. & Evans, R. C. Enhancing the stability of organolead halide perovskite films through polymer encapsulation. *RSC Adv.* **7**, 32942–32951 (2017).
19. Reichmanis, E., Frank, C. W., O'Donnell, J. H. & Hill, D. J. T. in *Irradiation of Polymeric Materials* (eds Reichmanis, E., Frank, C. W. & O'Donnell, J. H.) Vol. 527 ACS Symposium Series Ch. 1 (American Chemical Society, 1993).
20. Kirmani, A. R. et al. Countdown to perovskite space launch: guidelines to performing relevant radiation-hardness experiment. *Joule* https://doi.org/10.1016/j.joule.2022.03.004 (2022).
21. Durant, B. K. et al. Radiation stability of mixed tin–lead halide perovskites: implications for space applications. *Sol. Energy Mater. Sol. Cells* **230**, 111232 (2021).
22. Tong, J. et al. Carrier lifetimes of >1 μs in Sn–Pb perovskites enable efficient all-perovskite tandem solar cells. *Science* **364**, 475–479 (2019).
23. Beal, R. E. et al. Cesium lead halide perovskites with improved stability for tandem solar cells. *J. Phys. Chem. Lett.* **7**, 746–751 (2016).
24. He, J. et al. Surface chelation of cesium halide perovskite by dithiocarbamate for efficient and stable solar cells. *Nat. Commun.* **11**, 4237 (2020).
25. Luo, Y.-X. et al. Uniform stepped interfacial energy level structure boosts efficiency and stability of $CsPbI_2Br$ solar cells. *Adv. Funct. Mater.* **31**, 2103316 (2021).
26. Messenger, S. R., Summers, G. P., Burke, E. A., Walters, R. J. & Xapsos, M. A. Modeling solar cell degradation in space: a comparison of the NRL displacement damage dose and the JPL equivalent fluence approaches. *Prog. Photovolt. Res. Appl.* **9**, 103–121 (2001).
27. Ziegler, J. F., Ziegler, M. D. & Biersack, J. P. SRIM—the stopping and range of ions in matter (2010). *Nucl. Instrum. Methods Phys. Res. B* **268**, 1818–1823 (2010).
28. Saliba, M. et al. Cesium-containing triple cation perovskite solar cells: improved stability, reproducibility and high efficiency. *Energy Environ. Sci.* **9**, 1989–1997 (2016).
29. Messenger, S. R. et al. Effect of omnidirectional proton irradiation on shielded solar cells. *IEEE Trans. Nucl. Sci.* **53**, 3771–3778 (2006).
30. Walters, R. J., Warner, J. H., Messenger, S. R., Lorentzen, J. R. & Summers, G. P. in *2006 IEEE 4th World Conference on Photovoltaic Energy Conference* 1899–1902 (IEEE, 2006).
31. Anspaugh, B. E. in *The Conference Record of the Twenty-Second IEEE Photovoltaic Specialists Conference–1991* 1593–1598 (IEEE, 1991).
32. Insoo, J., Xapsos, M. A. & Burke, E. A. Alpha particle nonionizing energy loss (NIEL). *IEEE Trans. Nucl. Sci.* **51**, 3207–3210 (2004).
33. Brus, V. V. et al. Defect dynamics in proton irradiated $CH_3NH_3PbI_3$ perovskite solar cells. *Adv. Electron. Mater.* **3**, 1600438 (2017).
34. Jones, R. Alternative orbits: a new space solar power reference design. *Online J. Space Commun.* **9**, 14 (2021).
35. Jiang, Y. et al. Mitigation of vacuum and illumination-induced degradation in perovskite solar cells by structure engineering. *Joule* **4**, 1087–1103 (2020).
36. Li, Y. et al. Li dopant induces moisture sensitive phase degradation of an all-inorganic $CsPbI_2Br$ perovskite. *Chem. Commun.* **54**, 9809–9812 (2018).
37. Zhou, Y. & Zhao, Y. Chemical stability and instability of inorganic halide perovskites. *Energy Environ. Sci.* **12**, 1495–1511 (2019).
38. Ke, W. et al. Narrow-bandgap mixed lead/tin-based 2D Dion–Jacobson perovskites boost the performance of solar cells. *J. Am. Chem. Soc.* **142**, 15049–15057 (2020).
39. Li, C. et al. In situ tin(II) complex antisolvent process featuring simultaneous quasi-core–shell structure and heterojunction for improving efficiency and stability of low-bandgap perovskite solar cells. *Adv. Energy Mater.* **10**, 1903013 (2020).
40. Chang, C.-Y., Lee, K.-T., Huang, W.-K., Siao, H.-Y. & Chang, Y.-C. High-performance, air-stable, low-temperature processed semitransparent perovskite solar cells enabled by atomic layer deposition. *Chem. Mater.* **27**, 5122–5130 (2015).
41. Lee, Y. I. et al. A low-temperature thin-film encapsulation for enhanced stability of a highly efficient perovskite solar cell. *Adv. Energy Mater.* https://doi.org/10.1002/aenm.201701928 (2018).
42. Ramos, F. J. et al. Versatile perovskite solar cell encapsulation by low-temperature ALD-Al_2O_3 with long-term stability improvement. *Sustain. Energy Fuels* **2**, 2468–2479 (2018).
43. Matteocci, F. et al. Encapsulation for long-term stability enhancement of perovskite solar cells. *Nano Energy* **30**, 162–172 (2016).
44. Rout, B. et al. An overview of the facilities, activities, and developments at the University of North Texas Ion Beam Modification and Analysis Laboratory (IBMAL). *AIP Conf. Proc.* **1544**, 11–18 (2013).
45. Young, J. M. et al. Synthesis of magnesiowüstite nanocrystallites embedded in an amorphous silicate matrix via low energy multiple ion implantations. *Planet. Space Sci.* **206**, 105319 (2021).

Acknowledgements

This work was authored by NREL operated by the Alliance for Sustainable Energy, LLC, for the US Department of Energy (DOE) under contract no. DE-AC36-08GO28308. NREL acknowledges support from the Operational Energy Capability Improvement Fund (OECIF) of the US Department of Defense (DOD). B.R. acknowledges partial support from the National Science Foundation (NSF) grant no. HBCU-EiR-2101181. The work at the University of Oklahoma was supported by the National Aeronautics and Space Administration under agreement no. 80NSSC19M0140 issued through NASA Oklahoma EPSCoR. K.T.V. acknowledges the NASA Space Technology Mission Directorate's Early Career Initiative Program for support of this work. We thank R. Darling of the Office of the Undersecretary of Defense for Acquisition and Sustainment, Arlington for guidance and support. The views expressed in the article do not necessarily represent the views of the DOE or the US Government.

Author contributions

A.R.K. and J.M.L. conceived and supervised this work and wrote the manuscript. A.R.K. fabricated the solar cells, designed and carried out the stressing experiments and performed device characterization.

D.P.O. supported the SiO_x deposition and ambient characterization of Sn–Pb perovskite solar cells. K.T.V. supported the DC 93-500 encapsulation. K.N.H. and B.S. carried out α-irradiation at NREL. W.N. deposited the electrically insulating ITO barrier on the devices. J.T. and K.Z. fabricated the Sn–Pb perovskite solar cells for the study. T.A.B. and B.R. carried out proton and α-irradiation at the University of North Texas with suggestions and insight from I.R.S. B.R. supported the SRIM/TRIM simulations. R.C.B. sputtered ITO electrodes on quartz substrates for the solar cell fabrication. All the authors contributed to the discussion and editing of the paper.

Competing interests

A.R.K., D.P.O. and J.M.L. are inventors on a pending provisional patent (US patent 63/301,295 by Alliance for Sustainable Energy) related to protective barriers for space-based perovskite PVs as discussed in this manuscript. All the other authors declare no competing interests.

Additional information

Supplementary information The online version contains supplementary material available at https://doi.org/10.1038/s41560-022-01189-1.

Correspondence and requests for materials should be addressed to Ahmad R. Kirmani or Joseph M. Luther.

Peer review information *Nature Energy* thanks Romain Cariou, Felix Lang and the other, anonymous, reviewer(s) for their contribution to the peer review of this work.

nature research

Corresponding author(s): Joseph M. Luther, Ahmad R. Kirmani

Solar Cells Reporting Summary

Nature Research wishes to improve the reproducibility of the work that we publish. This form is intended for publication with all accepted papers reporting the characterization of photovoltaic devices and provides structure for consistency and transparency in reporting. Some list items might not apply to an individual manuscript, but all fields must be completed for clarity.

For further information on Nature Research policies, including our data availability policy, see Authors & Referees.

Experimental design

Please check: are the following details reported in the manuscript?

1. Dimensions			
Area of the tested solar cells	☒ Yes ☐ No	'J-V characterization' sub-section under 'Methods' section.
Method used to determine the device area	☒ Yes ☐ No	'J-V characterization' sub-section under 'Methods' section.
2. Current-voltage characterization			
Current density-voltage (J-V) plots in both forward and backward direction	☒ Yes ☐ No	'J-V characterization' sub-section under 'Methods' section.
Voltage scan conditions *For instance: scan direction, speed, dwell times*	☒ Yes ☐ No	'J-V characterization' sub-section under 'Methods' section.
Test environment *For instance: characterization temperature, in air or in glove box*	☒ Yes ☐ No	'J-V characterization' sub-section under 'Methods' section.
Protocol for preconditioning of the device before its characterization	☐ Yes ☒ No	Preconditioning not needed for these devices
Stability of the J-V characteristic *Verified with time evolution of the maximum power point or with the photocurrent at maximum power point; see ref. 7 for details.*	☐ Yes ☒ No	Stability and high efficiency are not the main focus of this paper
3. Hysteresis or any other unusual behaviour			
Description of the unusual behaviour observed during the characterization	☐ Yes ☒ No	Devices didn't exhibit any unusual behavior during characterization
Related experimental data	☐ Yes ☒ No	Devices didn't exhibit any unusual behavior during characterization
4. Efficiency			
External quantum efficiency (EQE) or incident photons to current efficiency (IPCE)	☒ Yes ☐ No	Supplementary Figure 11, Supplementary Table 1
A comparison between the integrated response under the standard reference spectrum and the response measure under the simulator	☐ Yes ☒ No	Record devices with high Jsc (current) values are not a focus of this paper
For tandem solar cells, the bias illumination and bias voltage used for each subcell	☐ Yes ☒ No	This paper does not report any tandem solar cells
5. Calibration			
Light source and reference cell or sensor used for the characterization	☒ Yes ☐ No	'J-V characterization' sub-section under 'Methods' section.
Confirmation that the reference cell was calibrated and certified	☒ Yes ☐ No	'J-V characterization' sub-section under 'Methods' section.

Calculation of spectral mismatch between the reference cell and the devices under test	☒ Yes ☐ No	'J-V characterization' sub-section under 'Methods' section.

6. Mask/aperture

Size of the mask/aperture used during testing	☒ Yes ☐ No	'J-V characterization' sub-section under 'Methods' section.
Variation of the measured short-circuit current density with the mask/aperture area	☐ Yes ☒ No	Device performance as a function of mask area is not the focus of this paper

7. Performance certification

Identity of the independent certification laboratory that confirmed the photovoltaic performance	☐ Yes ☒ No	This paper does not report record solar cell efficiencies
A copy of any certificate(s) *Provide in Supplementary Information*	☐ Yes ☒ No	This paper does not report record solar cell efficiencies

8. Statistics

Number of solar cells tested	☒ Yes ☐ No	Captions of Figures 1, 2, 4, Table 1, Supplementary Figures 1, 7, 9
Statistical analysis of the device performance	☒ Yes ☐ No	Table 1

9. Long-term stability analysis

Type of analysis, bias conditions and environmental conditions *For instance: illumination type, temperature, atmosphere humidity, encapsulation method, preconditioning temperature*	☐ Yes ☒ No	Stability and high efficiency are not the main focus of this paper

nature energy

Article

https://doi.org/10.1038/s41560-022-01189-1

Metal oxide barrier layers for terrestrial and space perovskite photovoltaics

In the format provided by the authors and unedited

Table of Contents

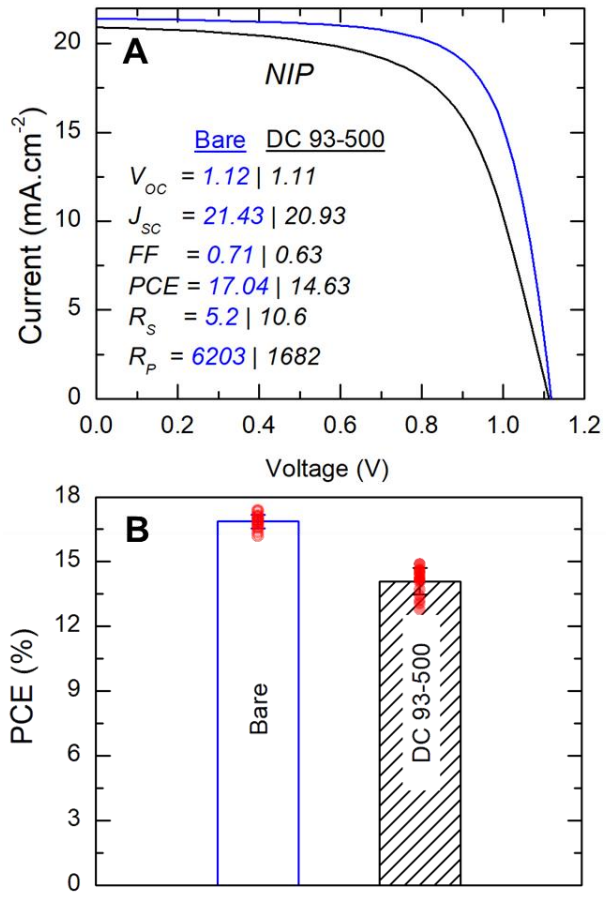

Supplementary Figure 1. Effect of DC 93-500 encapsulation schemes on device performance. The deleterious effect of the space-grade DC 93-500 silicone elastomer encapsulant on *NIP* triple-cation cells. Data in (B) is based on 16 devices for each category which are depicted by red circles overlayed on the bars. Error bars represent standard deviation. While the series resistance (R_S) increases after DC 93-500 encapsulation from 5.2 Ω.cm^{-2} to 10.6 Ω.cm^{-2}, the shunt resistance (R_P) undergoes a reduction from 6203 Ω.cm^{-2} to 1682 Ω.cm^{-2}. These changes cause a reduction in the fill-factor (FF). This likely happens because of a chemical or mechanical modification of the device stack upon application of DC 93-500. The silicone elastomer and the solvent can either chemically interact with the device stack or can exert mechanical strain on it during the drying process. Information on the exact chemical composition of this elastomer has not been made readily available by the supplier due to proprietary constraints.

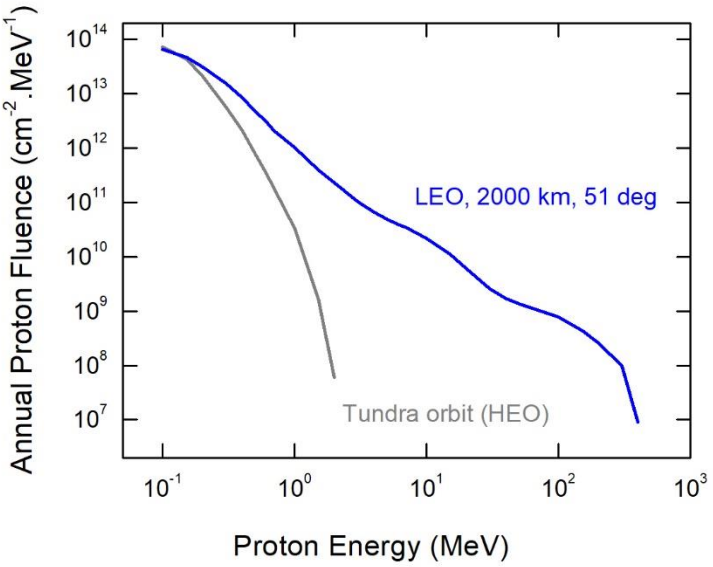

Supplementary Figure 2. Proton environments in LEO and Tundra orbits.
Differential proton fluence for a 1-yr mission in a LEO orbit (blue) and a Tundra orbit (grey).

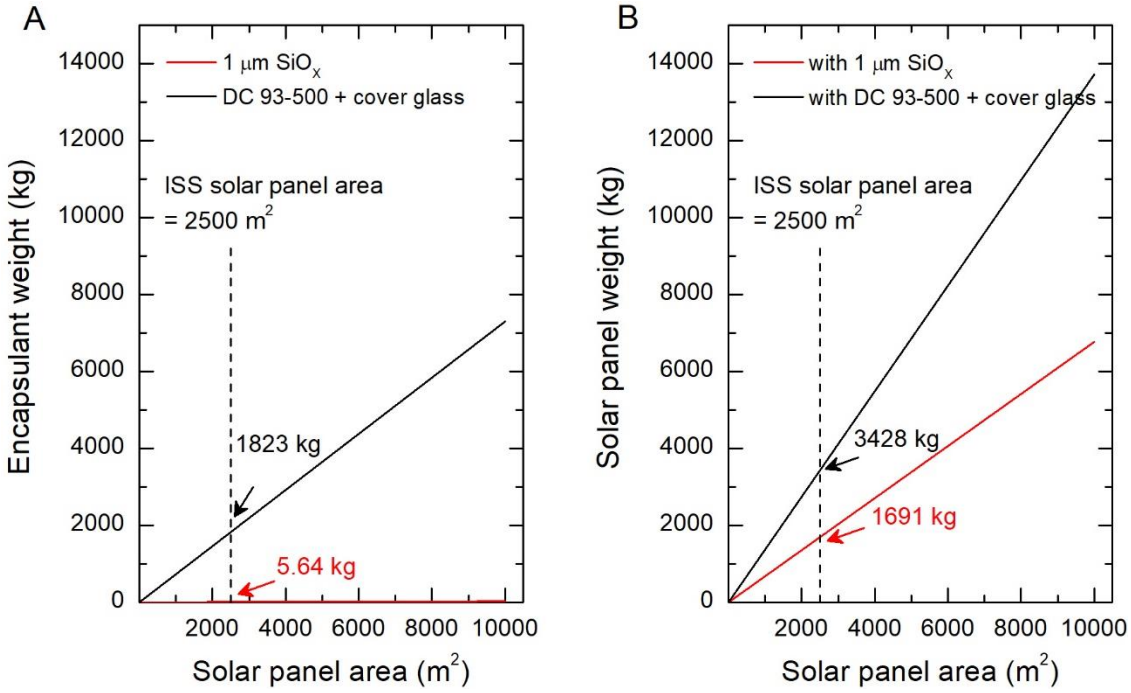

Supplementary Figure 3. Weight benefit of SiO_X encapsulation.
(A) Comparison between encapsulant weights for DC 93-500 and cover glass (black), and 1 μm SiO_X. SiO_X results in 99.7% encapsulant weight reduction. (B) Comparison of perovskite solar panel weights as a function of the panel area using DC 93-500 and cover glass (black), and 1 μm SiO_X (red) encapsulation schemes. Weights were measured on solar cells fabricated on ultrathin Ceria-doped borosilicate glass substrates using the two encapsulation techniques. These weights

were then extrapolated to larger panel areas. An area of 2500 m^2 corresponds to the solar arrays powering the International Space Station (ISS). SiO_X reduces the panel weight by 50.7%.

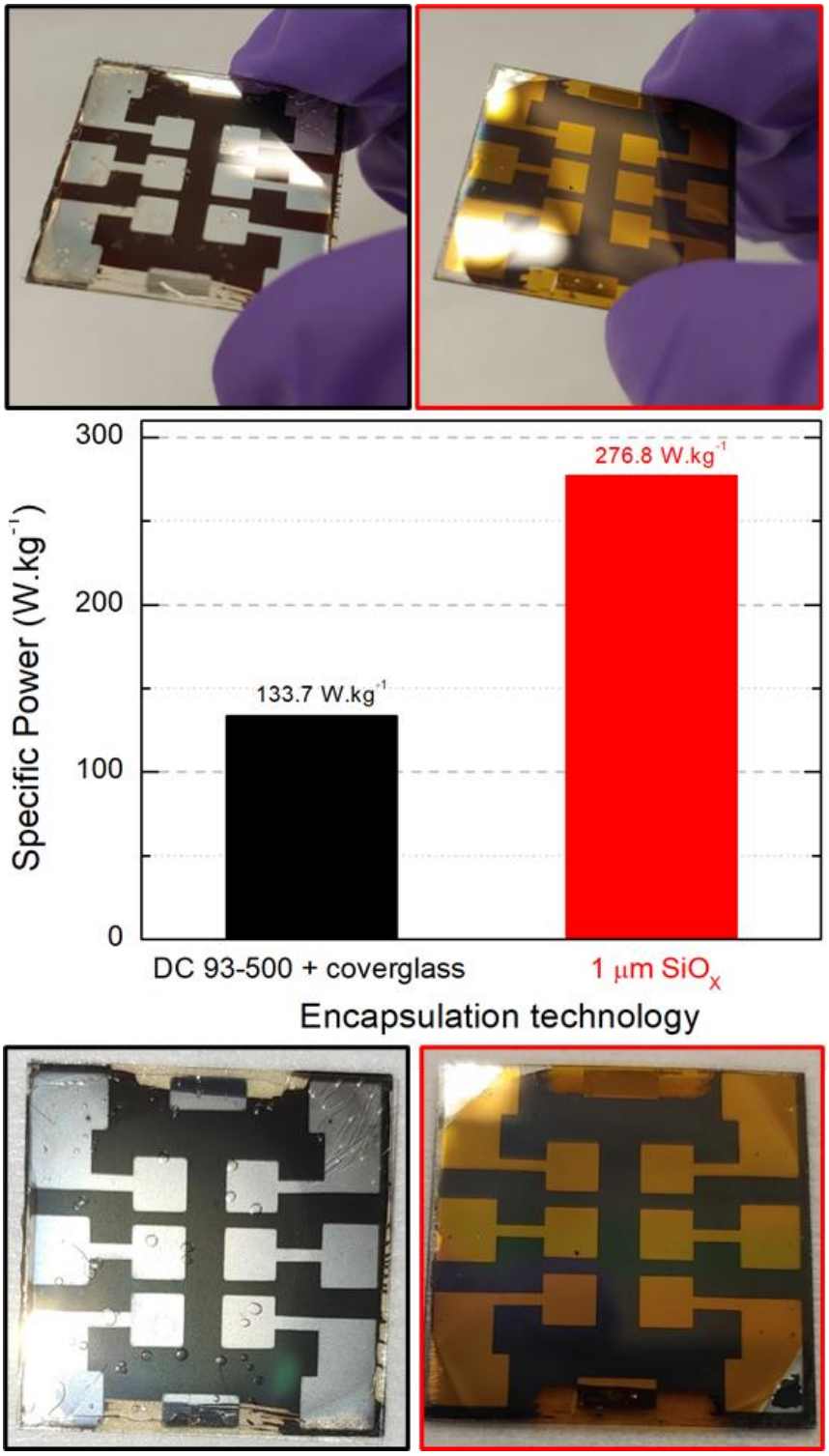

Supplementary Figure 4. Specific power advantage of SiO_X encapsulation.
Specific powers were measured for perovskite solar cells fabricated on lightweight Ceria-doped borosilicate glass substrates 250 μm thickness, using 'DC 93-500 + cover glass' encapsulation scheme (black) and SiO_X scheme (red). Bare cells without any encapsulation were found to weigh ~400 mg. For the DC 93-500 scheme, ~60 mg DC 93-500 was required to fully cover the solar cell. This was then covered with a ~400 mg of Ceria-doped borosilicate cover glass from the top. Despite the care, it is usual for this encapsulation technique to result in air bubbles (see photo) that can cause rupture of cover glass in space due to vacuum. For the SiO_X encapsulation scheme, the weight of 1 μm SiO_X was measured to be 1.45 mg, which is close to the theoretically determined value of 1.37 mg considering a mass density of 2.13 $g.cm^{-3}$. Initial device PCEs were found to be ~18.5%, not considering the slight loss in performance that happens after DC 93-500 encapsulation. Using this output power and factoring in the experimentally measured device weights, a specific power of 133.7 $W.g^{-1}$ was determined for the 'DC 93-500 + cover glass' encapsulated devices. For the SiO_X encapsulated device, a 107% increase in the specific power to 276.8 $W.g^{-1}$ was found. It is important to note here that we ensured full coverage of the cells with the encapsulants without leaving edges exposed for electrical contact. This was done to get a precise estimate on the encapsulant weights.

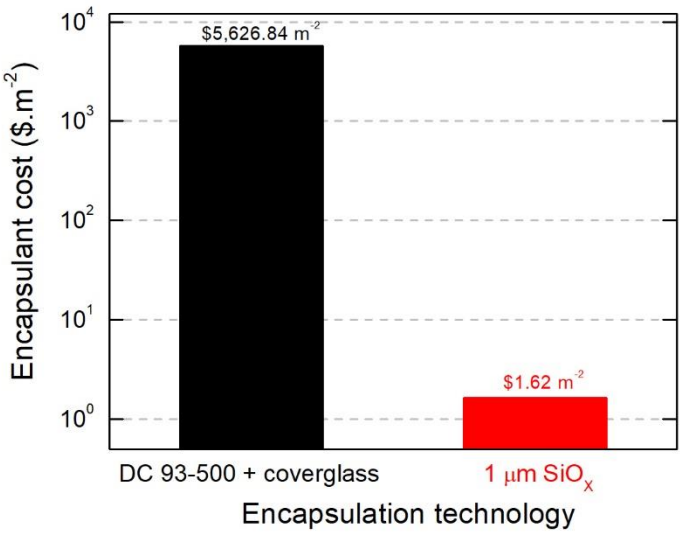

Supplementary Figure 5. Cost benefit of SiO_X encapsulation.
Cost analysis for the 'DC 93-500 + cover glass' and 1 μm SiO_X encapsulation technologies. Price data was acquired from the materials suppliers of DC 93-500, Ceria-doped borosilicate glass, and SiO_X. The cost model considered a square meter of solar panel area and costs of encapsulation material required. SiO_X is found to offer a 99.97% reduction in materials costs. It is expected that the deposition techniques used and the rate of deposition of these encapsulants will further enhance the cost contrasts. While SiO_X can be deposited using the industry-compatible thermal evaporation technique at deposition rates >10 $nm.min^{-1}$, the 'DC 93-500 + cover glass' scheme is a slow process requiring extreme care and time to ensure complete coverage of the device area.

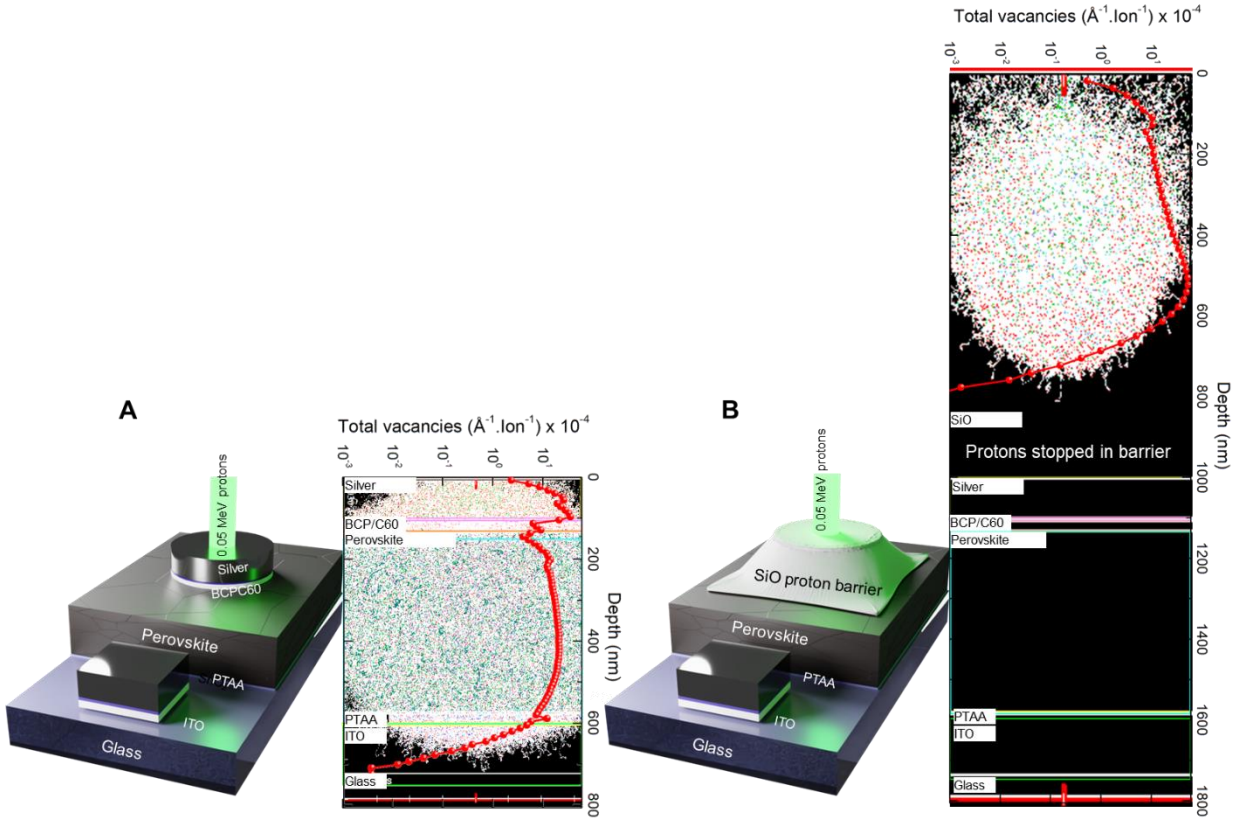

Supplementary Figure 6. SRIM/TRIM simulations for 0.05 MeV protons on *PIN* cells. Theoretical simulations showing interaction of 0.05 MeV protons with a *PIN* triple-cation solar cell (A) without, and (B) 1 μm SiO_X barrier.

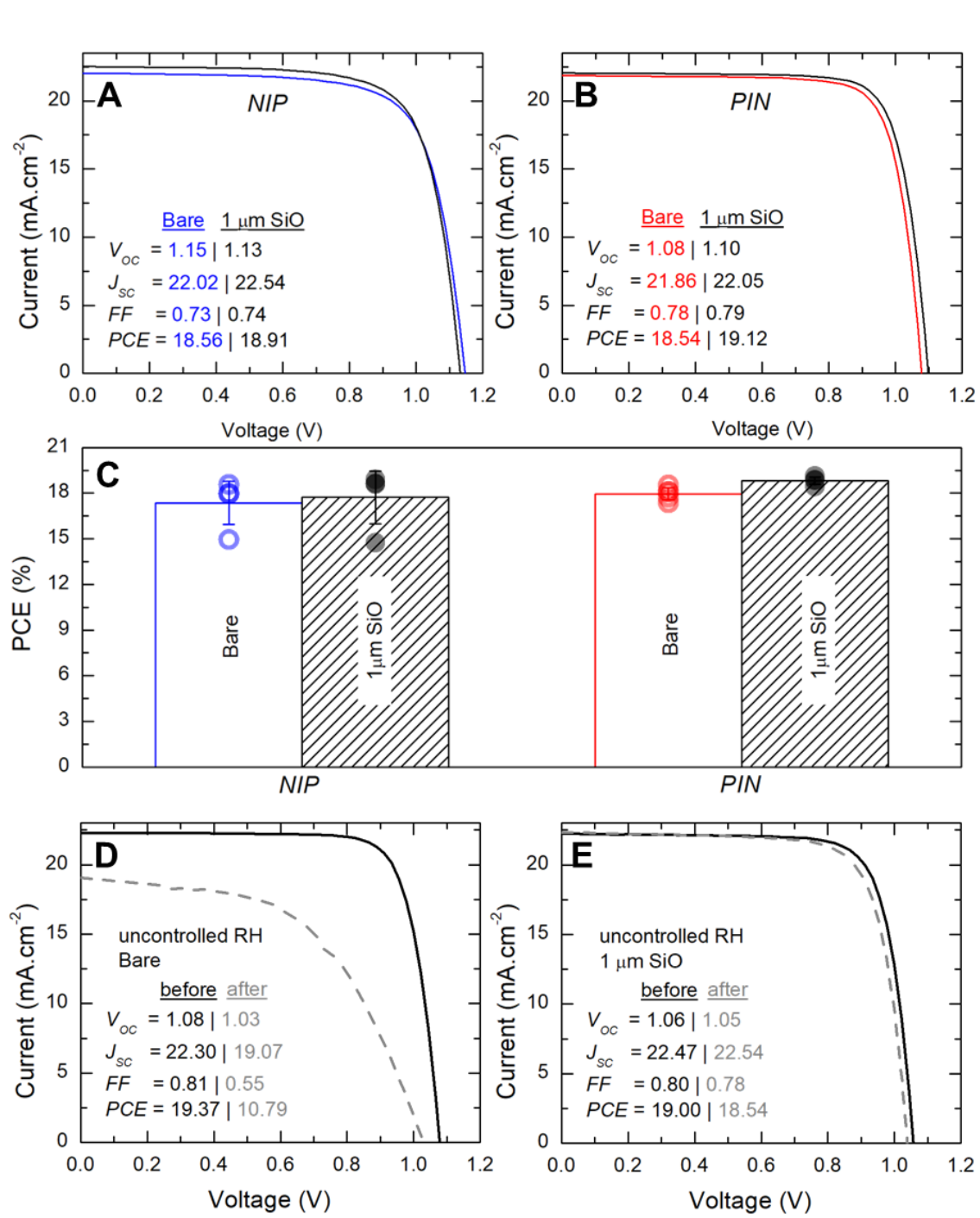

Supplementary Figure 7. Effect of SiO_X encapsulation on device performance.
J-V curves for bare and protected triple-cation solar cells in (A) *NIP*, and (B) *PIN* configuration. (C) Bar graphs showing the effect on PCEs after 1 μm SiO_X deposition. Averages were performed over 4 and 5 devices for the *NIP* and *PIN* cells, respectively, depicted by circles overlayed on the bars. Error bars represent standard deviation. *PIN* solar cells were exposed to an uncontrolled moisture environment for a period of multiple days. While the bare devices underwent degradation, 1 μm SiO_X protected cells showed no noticeable PCE change. *J-V* curves for devices exposed to

uncontrolled moisture and temperature are shown in (D) and (E) for the bare and 1 μm SiO_X protected cells.

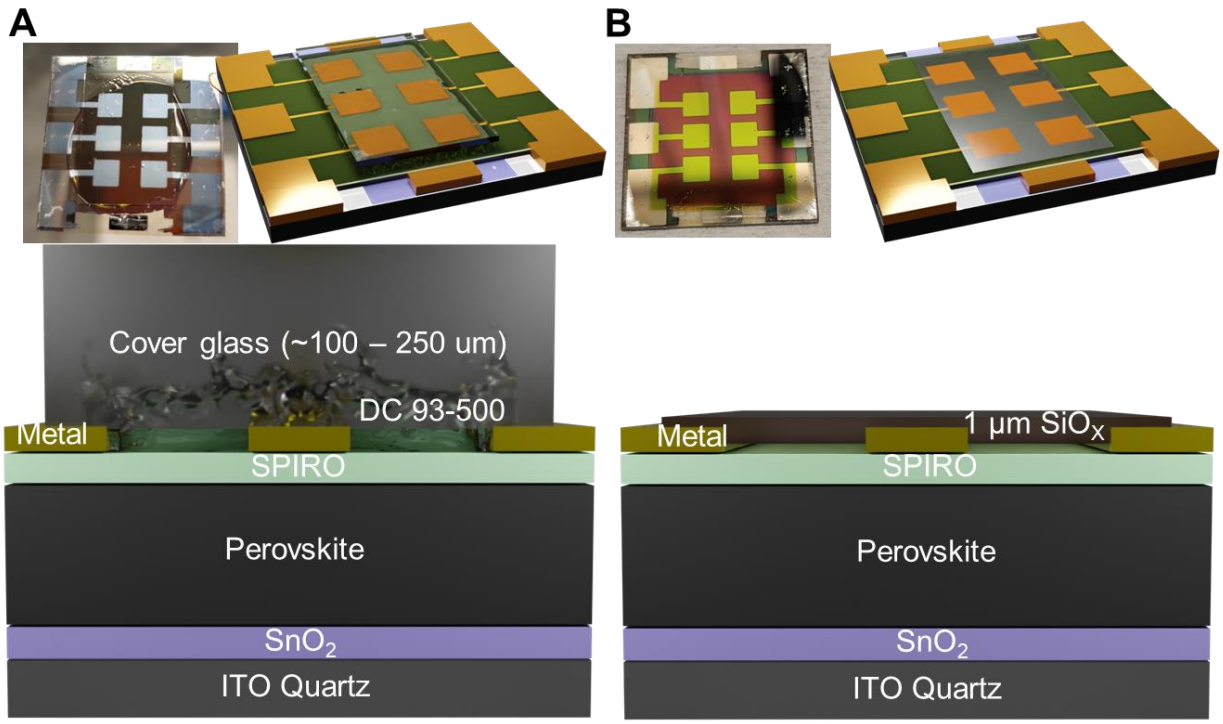

Supplementary Figure 8. Schematic illustration of DC 93-500 and SiO_X encapsulation schemes.
Schematics showing a perovskite solar cell encapsulated with (A) DC 93-500 and cover glass, and (B) with SiO_X barrier. Photos of representative devices are included in insets. Cross-sectional schematics are also shown for each case with the various layers in the device stacks. Light is incident from the quartz side (bottom).

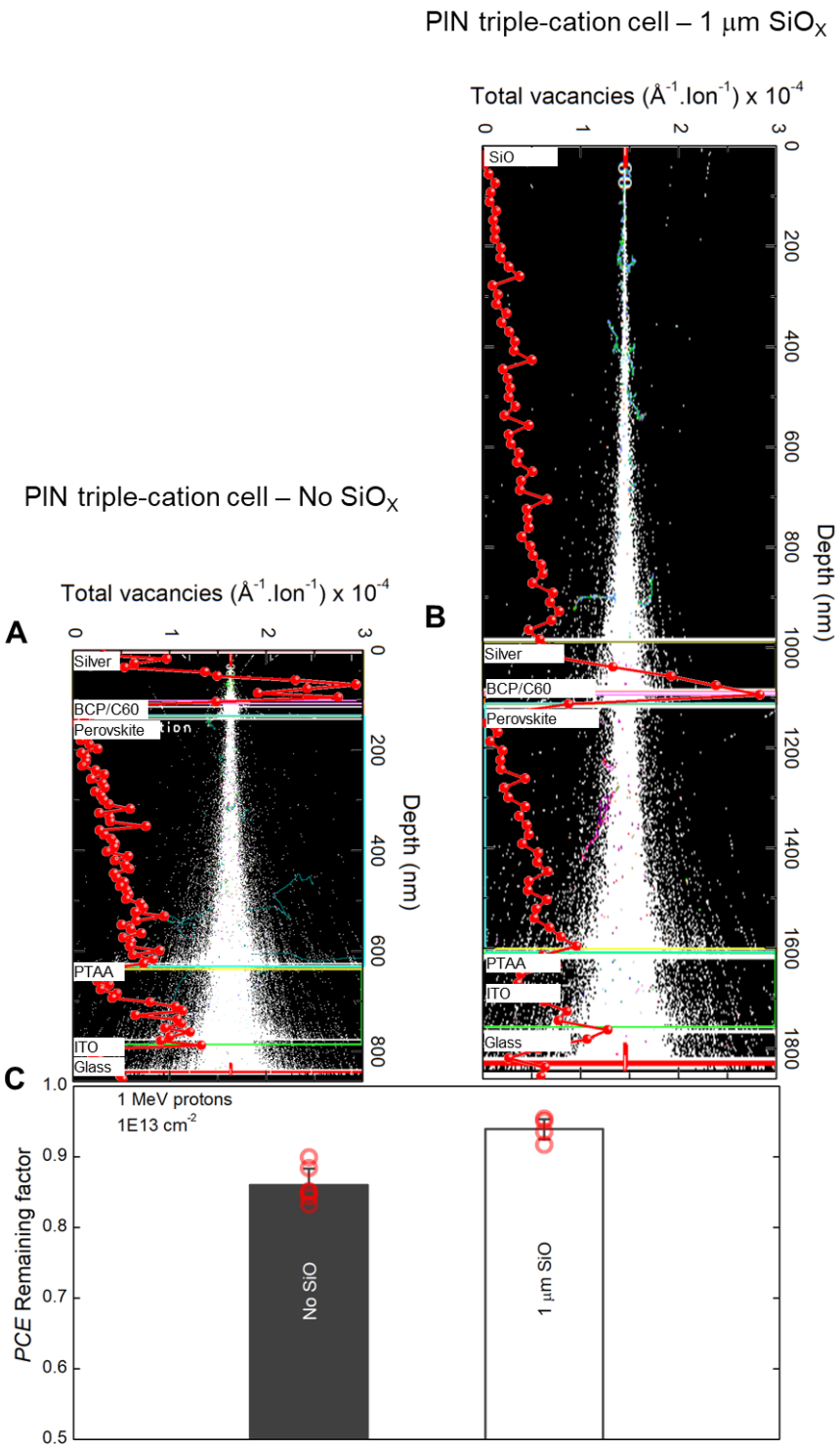

Supplementary Figure 9. SRIM/TRIM simulations for 1.0 MeV protons on *PIN* cells.
1 MeV proton irradiation of PIN triple-cation cells. SRIM/TRIM simulations showing straggling of 1 MeV protons in PIN perovskite solar cells (A) without, and (B) a 1 μm SiO_X barrier. Damage profiles within the solar cell are found to be the same across the two architectures, however, C) an increase in PCE remaining factor is observed for the SiO_X-protected device. Given the high IEL

associated with 1 MeV protons, the bare cell also has a higher remaining factor likely due to the self-healing mechanism involved with IEL. Sample sizes for the 'No SiO' and '1 μm SiO' cells are 6 and 4, respectively. Individual datapoints are depicted by red circles overlayed on the bars. Error bars represent standard deviation.

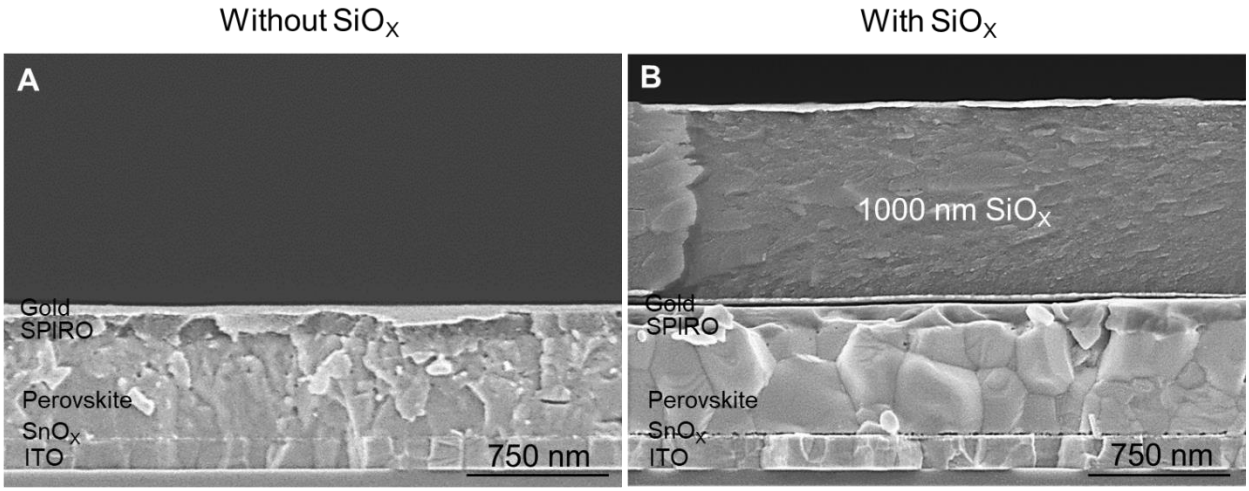

Supplementary Figure 10. X-SEM evidence of proton damage in the device stack.
X-SEM images of *NIP* triple-cation solar cells (A) without, and (B) with SiO_X barrier, irradiated with 0.05 MeV protons at a fluence of 10^{15} cm^{-2}. Proton irradiation leads to severely disrupted microstructure in the bare solar cell, while SiO_X protects the device stack from radiation damage. The bare device showed complete damage (0% PCE), while the SiO_X-capped device showed no drop from its initial PCE.

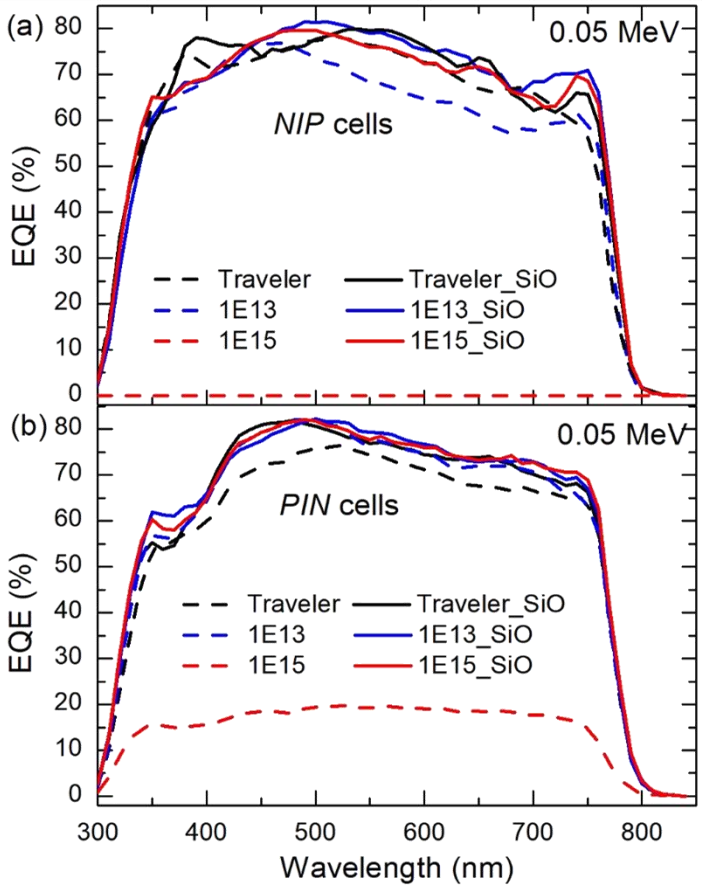

Supplementary Figure 11. EQE spectra on irradiated cells.
EQE data on (A) *NIP*, and (B) *PIN* triple-cation solar cells irradiated with different fluences of 0.05 MeV protons. Data for both bare (dashed lines) and protected (solid lines) are shown.

Supplementary Table 1.
Integrated J_{SC} values for solar cells irradiated with 0.05 MeV protons calculated from EQE spectra shown in Figure S11. EQE spectra were used as supporting evidence to show the changes occur across the whole spectrum rather than for specific wavelengths. Data from AM 1.5G measurements shown in Table 1 is based on an NREL-calibrated Si photodiode provides a more accurate representation of the J_{SC} trends.

Architecture	0.05 MeV proton fluence (cm^{-2})	Int. J_{SC} ($mA.cm^{-2}$)
*NIP*_without SiO_X	10^{13}	16.66
	10^{15}	0
*NIP*_with 1 µm SiO_X	10^{13}	18.86
	10^{15}	18.40
*PIN*_without SiO_X	10^{13}	18.58
	10^{15}	4.56
*PIN*_with 1 µm SiO_X	10^{13}	18.97
	10^{15}	19.02

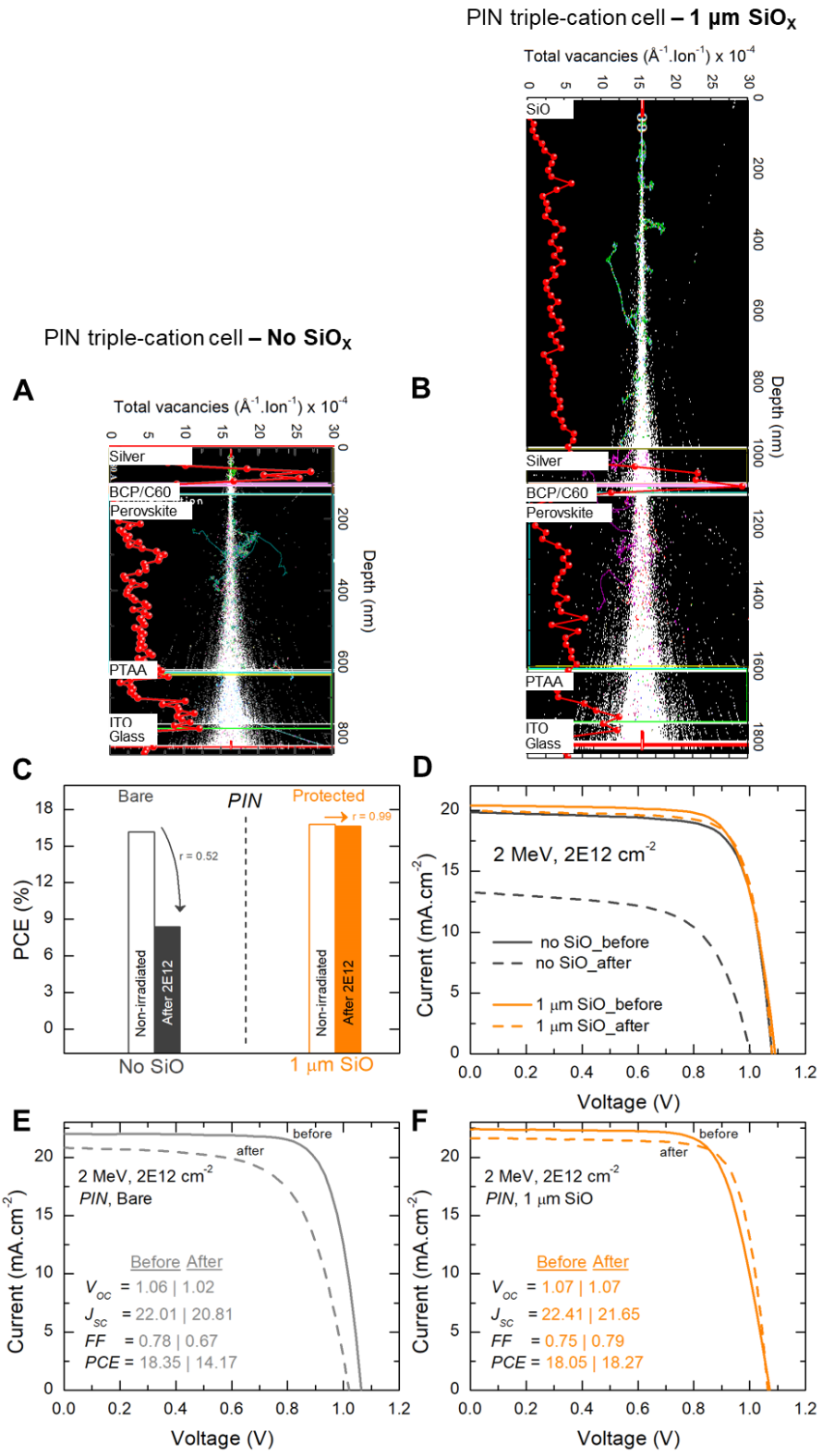

Supplementary Figure 12. SRIM/TRIM simulations for 2.0 MeV α-particles on *PIN* cells. *α-irradiation of PIN triple-cation cells.* SRIM/TRIM simulations for 2 MeV α-particles incident on a *PIN* triple-cation solar cell (A) without, and (B) with 1 µm SiO_X. (C) Effect of α-irradiation

using the RBS setup on the PCEs, and (D) corresponding *J-V* curves. Results of α-irradiation carried out at IBL, University of North Texas are shown in (E) and (F).

Supplementary Note 1: Cumulative DDD and Lifetime calculations

1-year differential proton fluences for the various orbits were obtained by simulating the orbits in SPENVIS.[1] Next, considering the stopping powers of 1 μm SiO_X from SRIM/TRIM, slowed proton fluences were calculated. NIEL values for various proton energies were calculated for the triple-cation solar cells using SPENVIS. NIEL calculations were carried out using SPENVIS and further verified using SR-NIEL.[2] Both codes calculate NIEL of a defined chemistry using a screened relativistic treatment for elastic Coulombic interactions between the incident particles and the target. Besides the chemical composition of the target, these codes require the displacement threshold energy for each element in the target as input parameters. We used the energies from SRIM: C = 28 eV, H = 10 eV, N = 28 eV, O = 28 eV, Cs = 25 eV, Pb = 25 eV, I = 25 eV, Br = 25 eV. In a previous report, we have calculated NIELs for various materials using these codes. Although NIELs for perovskite semiconductors have not yet been published by other researchers, the Si and III-V NIELs we calculated are in full agreement with previously published curves justifying the model used by SPENVIS and SR-NIEL.

Cumulative DDD was calculated as follows:

Cumulative displacement damage dose for a given orbit, $\int DDD = \int N_P(E) \cdot NIEL(E) \cdot dE,$ over the entire proton energy range for that orbit, where $N_P(E)$ is the fluence of protons at energy E, and $NIEL(E)$ is the proton NIEL at energy E, as described in Messenger et al.[3]

Lifetime in the orbit can then be calculated by computing the DDD for the particle energy E_0 used for irradiation, $DDD(E_0) = N_P(E_0) \cdot NIEL(E_0)$, and dividing it by $\int DDD$

Lifetime (years) = $DDD(E_0)/\int DDD$

For example, 0.05 MeV proton irradiation at a fluence of 10^{13} cm^{-2} results in a dose, $DDD(0.05\ p)$ = 3.9E12 $MeV.g^{-1}$, and corresponds to 0.06 years in GEO which has a $\int DDD$ of 6.57E13 $MeV.g^{-1}$.

Since the SiO_X layer fully blocks the 0.05 MeV protons, we sought to irradiate the solar cells with fully-penetrating protons to calculate the device's lifetime in orbit. We are specifically

interested in quantifying the impact of those fully penetrating particles that do not simultaneously cause healing. High-energy fully penetrating protons have been shown to cause healing and increase in device performance due to the higher ionizing energy loss (IEL) associated with them.[4,5] In general, particles with a lower value of IEL/NIEL ratio should be used for testing the radiation tolerance of perovskite solar cells. Figure S8 compares the IEL/NIEL ratio for 2 MeV protons and 2 MeV α-particles. Given their larger mass, α-particles are the most damaging radiation in space with a lower IEL and significantly higher NIEL values than protons, resulting in a relatively lower IEL/NIEL ratio. We therefore considered 2 MeV α for the lifetime calculation. 2 MeV α-particles at a fluence of 2.0×10^{12} cm^{-2} with DDD (2.0 α) = 7.8×10^{11} $MeV.g^{-1}$ led to a 50% degradation in device performance, while the SiO_X-capped cells retained 90% of their original PCE after irradiation with 2.0×10^{13} cm^{-2} fluence of 2 MeV α-particles. DDD for various particle energies and fluences are shown in Table S1 and the resulting increase in device lifetimes for various orbits is summarized in Table S2.

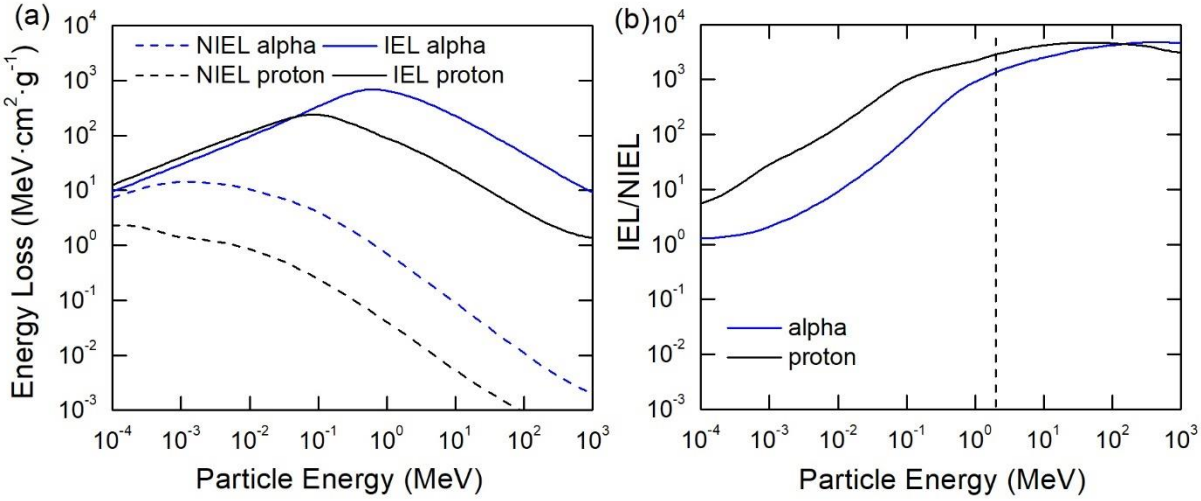

Supplementary Figure 13. NIEL and IEL profiles for protons and α-particles.
(A) NIEL and IEL for protons (black) and α-particles (blue) calculated for various particle energies using SR-NIEL.[2] (B) IEL/NIEL ratio for protons (black) and α-particles (blue). The dashed line indicates 2 MeV.

Supplementary Table 2.
DDD for various particle energies and fluences.

DDD ($MeV.g^{-1}$)	Fluence (cm^{-2})			
	10^{12}	10^{13}	10^{14}	10^{15}
0.05 p^+	3.9E11	3.9E12	3.9E13	3.9E14
2.0 α^+	3.9E11	3.9E12	3.9E13	3.9E14

Supplementary Table 3.
Cumulative DDD for the bare and SiO_X protected devices, and the calculated lifetimes.

	LEO (ISS)	LEO (2000 km)	5000 km	GEO	Juno
$\int DDD$ – bare	2.76E9	2.65E12	3.48E13	6.57E13	7.29E11
$\int DDD$ – 1 μm SiO_X	1.65E9	1.34E12	1.80E13	1.85E13	6.29E11
Reduction in $\int DDD$	40%	49%	48%	72%	14%
Lifetime bare cell(years)	282.61	0.29	0.02	0.01	1.07
Lifetime 1 μm SiO_X cell (years)	4727.27	5.81	0.43	0.42	12.40

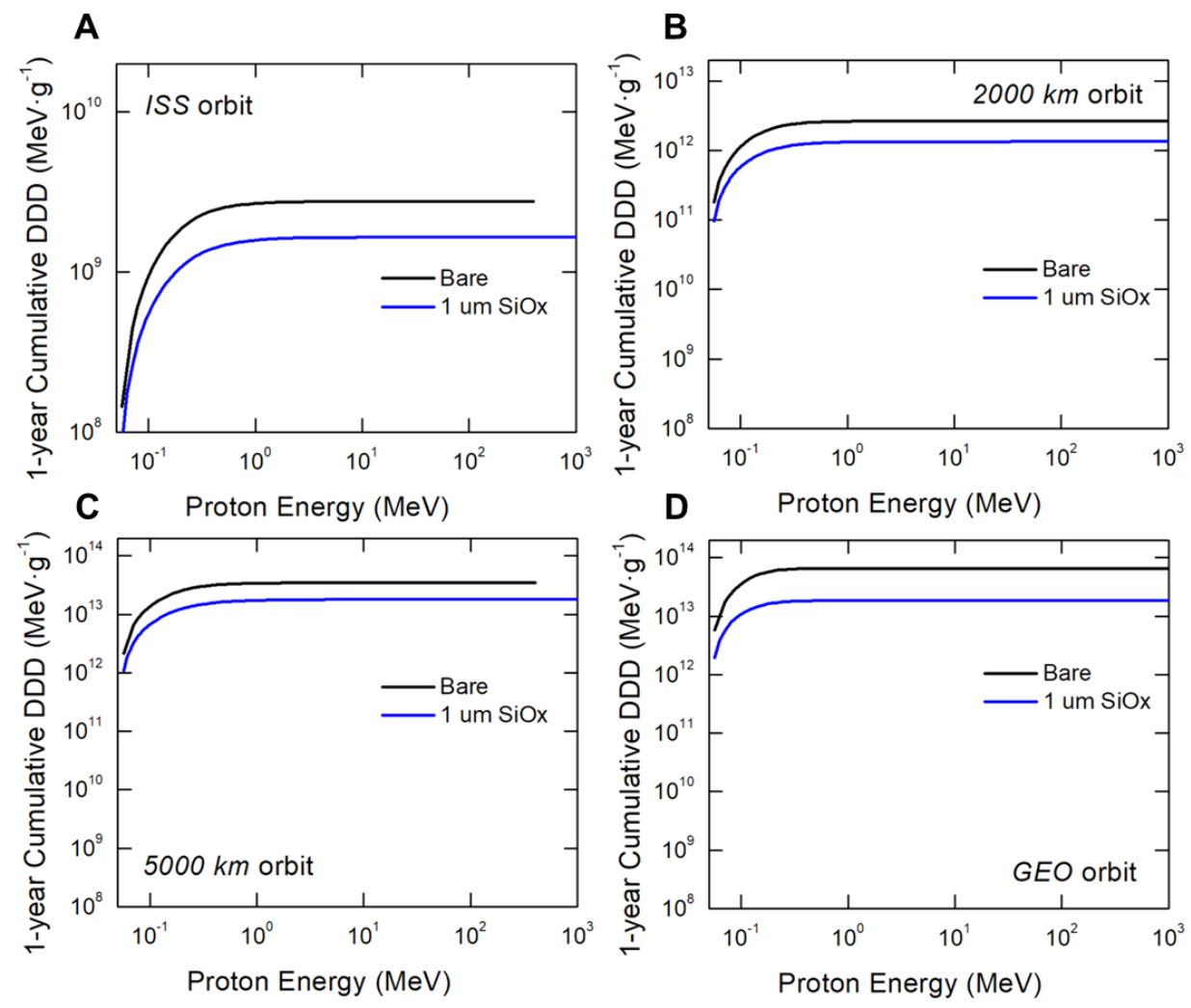

Supplementary Figure 14. Cumulative DDD calculations for various orbits.
1-year cumulative DDD for various orbits comparing the cases of a bare (black) and 1 μm SiO_X protected (blue) solar cells.

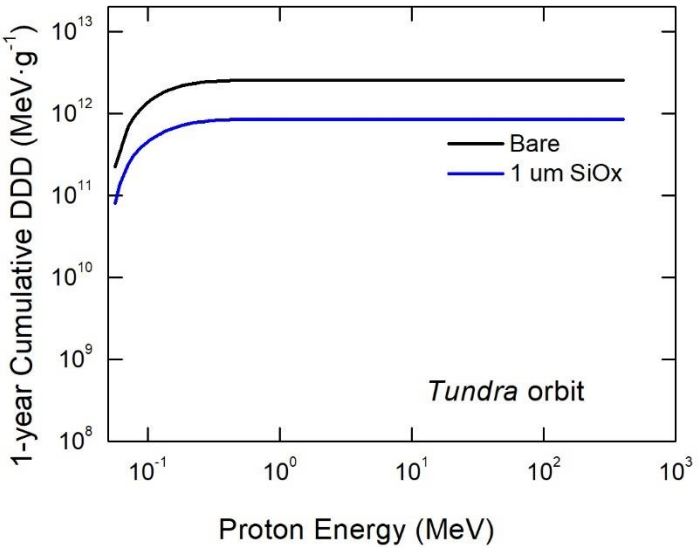

Supplementary Figure 15. Cumulative DDD calculation for the Tundra orbit.
1-year cumulative DDD for the Tundra orbit comparing the cases of a bare (black) and 1 μm SiO_X protected (blue) solar cells.

Supplementary Table 4.
Cumulative DDD for the bare and SiO_X protected devices, and the calculated lifetime for the Tundra orbit.

	Tundra
$\int DDD$ – bare	2.49E12
$\int DDD$ – 1 um SiO_X	7.97E11
Reduction in $\int DDD$	68%
Lifetime bare cell(years)	0.31
Lifetime 1 μm SiO_X cell (years)	9.79

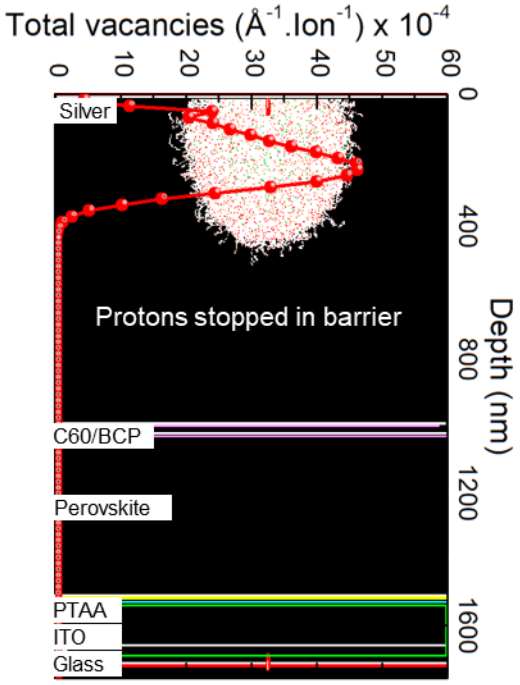

Supplementary Figure 16. SRIM/TRIM simulation on a 1000 μm Silver capped PIN cell. SRIM/TRIM simulation on a perovskite solar cell capped with a 1000 μm barrier of Silver. Simulation was carried out for 0.05 MeV protons and all protons were found to be blocked within 300 nm of the barrier.

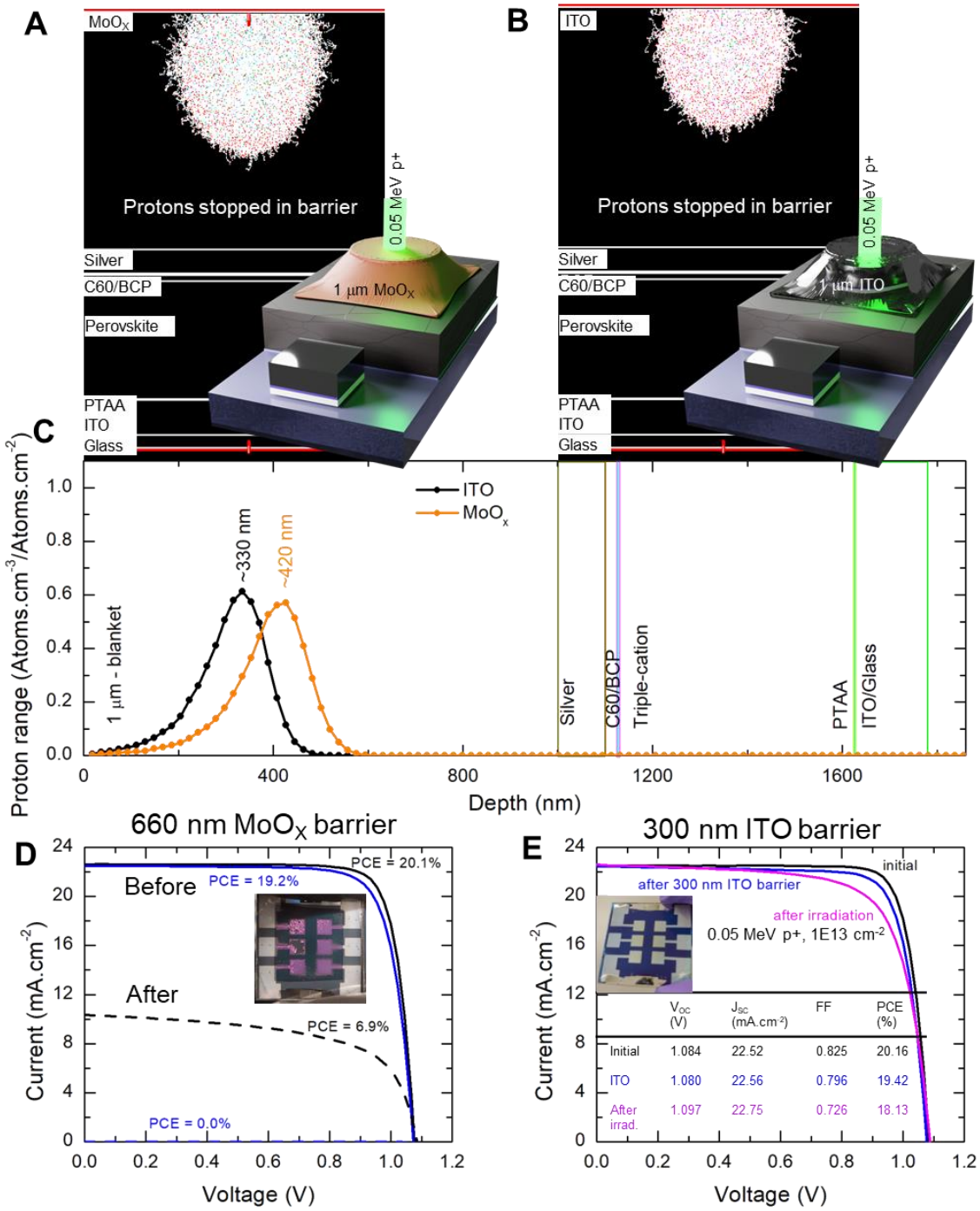

Supplementary Figure 17. SRIM/TRIM simulations for MoO_X and ITO barriers. SRIM/TRIM simulations showing straggling of 0.05 MeV protons in 1 um barriers of (A) MoO_X, and (B) ITO atop perovskite solar cells. (C) Proton ranges are found to be 420 nm and 330 nm in MoO_X and ITO, respectively. These layers were deposited via thermal evaporation (MoOx) and sputtering (ITO). (D) While significant device degradation was observed for MoO_X, (E) ITO barrier only resulted in a slight performance drop.

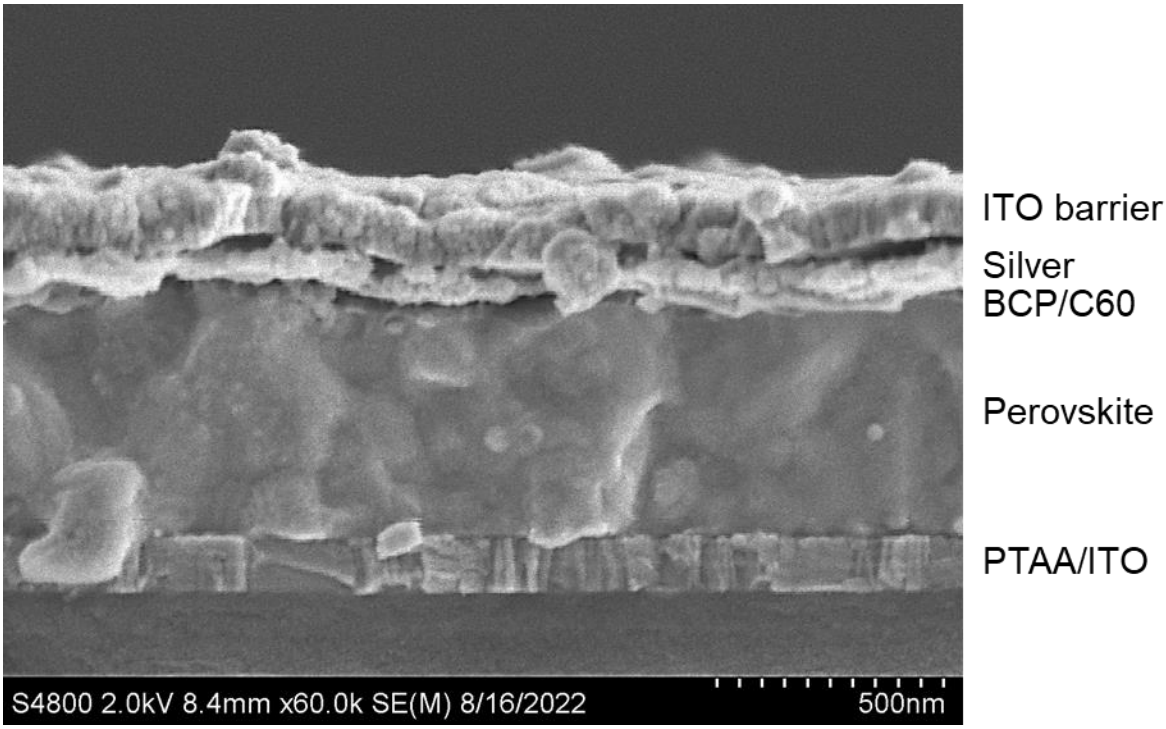

Supplementary Figure 18. X-SEM of a cell with ITO barrier.
X-SEM image showing a less uniform ITO barrier as compared to SiO_X shown in Figure 1D.

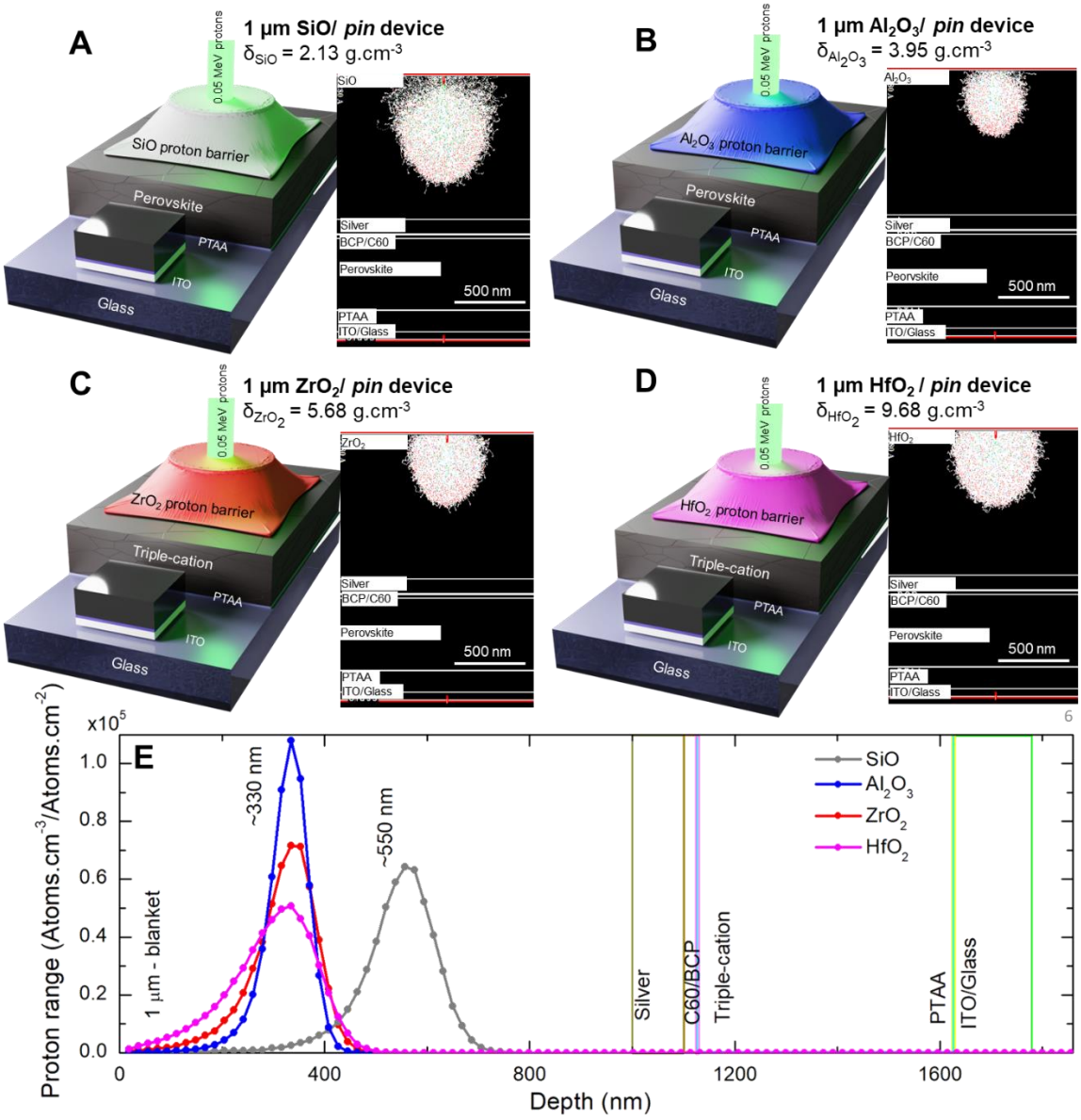

Supplementary Figure 19. SRIM/TRIM simulations for various oxide barriers.
Oxide barrier library: Simulated proton straggling for various 1 µm thick oxide proton barriers on *PIN* triple-cation devices. Proton ranges for each case are shown in (E).

Supplementary Table 5.
Comparison of the metal oxide barriers proposed and simulated in this work besides the experimentally explored SiO_X, MoO_X, and ITO.

Oxide	Deposition	Temperature	Rate	0.05 MeV Proton stopping range	Availability in standard processing
Al_2O_3	ALD/e-beam	~80-90 °C	~0.4-0.8 nm.min^{-1}	~330 nm	Common
ZrO_2	ALD/e-beam	~80-90 °C	~0.4-0.8 nm.min^{-1}	~340 nm	Rare
HfO_2	ALD/e-beam	~80-90 °C	~0.4-0.8 nm.min^{-1}	~330 nm	Rare

Supplementary References:

1 https://www.spenvis.oma.be/.

2 https://sr-niel.org/.

3 Messenger, S. R., Summers, G. P., Burke, E. A., Walters, R. J. & Xapsos, M. A. Modeling solar cell degradation in space: A comparison of the NRL displacement damage dose and the JPL equivalent fluence approaches†. *Progress in Photovoltaics: Research and Applications* **9**, 103-121, doi:https://doi.org/10.1002/pip.357 (2001).

4 Durant, B. K. *et al.* Tolerance of Perovskite Solar Cells to Targeted Proton Irradiation and Electronic Ionization Induced Healing. *ACS Energy Letters* **6**, 2362-2368, doi:10.1021/acsenergylett.1c00756 (2021).

5 Brus, V. V. *et al.* Defect Dynamics in Proton Irradiated CH3NH3PbI3 Perovskite Solar Cells. *Advanced Electronic Materials* **3**, 1600438, doi:https://doi.org/10.1002/aelm.201600438 (2017).